© 2021. Published by The Company of Biologists Ltd | Development (2021) 148, dev199551. doi:10.1242/dev.199551

HUMAN DEVELOPMENT

RESEARCH ARTICLE

Characterization and staging of outer plexiform layer development in human retina and retinal organoids

Sumitha Prameela Bharathan[1,2], Angela Ferrario[1], Kayla Stepanian[1], G. Esteban Fernandez[2], Mark W. Reid[1], Justin S. Kim[1], Chloe Hutchens[1], Narine Harutyunyan[1,2], Carolyn Marks[3], Matthew E. Thornton[4], Brendan H. Grubbs[4], David Cobrinik[1,2,5,6,7], Jennifer G. Aparicio[1,2] and Aaron Nagiel[1,2,5,*]

ABSTRACT

The development of the first synapse of the visual system between photoreceptors and bipolar cells in the outer plexiform layer (OPL) of the human retina is crucial for visual processing but poorly understood. By studying the maturation state and spatial organization of photoreceptors, depolarizing bipolar cells and horizontal cells in the human fetal retina, we establish a pseudo-temporal staging system for OPL development that we term OPL-Stages 0 to 4. This was validated through quantification of increasingly precise subcellular localization of bassoon to the OPL with each stage (P<0.0001). By applying these OPL staging criteria to human retinal organoids (HROs) derived from human embryonic and induced pluripotent stem cells, we observed comparable maturation from OPL-Stage 0 at day 100 in culture up to OPL-Stage 3 by day 160. Quantification of presynaptic protein localization confirmed progression from OPL-Stage 0 to 3 (P<0.0001). Overall, this study defines stages of human OPL development through mid-gestation and establishes HROs as a model system that recapitulates key aspects of human photoreceptor-bipolar cell synaptogenesis *in vitro*.

KEY WORDS: Human fetal retina, Human retinal organoid, Outer plexiform layer, Photoreceptor, Bipolar cell, Ribbon synapse

INTRODUCTION

Sensory processing in the visual system is dependent on the cellular and synaptic architecture of the retina (Hoon et al., 2014). The seven major cell types comprising the human retina are organized into three cell layers, with their synaptic terminals interacting at two plexiform layers (Dowling, 2009). The first synapse of the visual system is formed at the outer plexiform layer (OPL), between the cone and rod photoreceptors in the outer nuclear layer (ONL) and the horizontal cells (HCs) and bipolar cells (BCs) in the inner nuclear layer (INL) (Mumm et al., 2005). Study of the OPL provides an opportunity to understand key aspects of neuronal development and synaptogenesis given the demands of appropriately wiring four photoreceptor subtypes with approximately 15 BC subtypes (Cao et al., 2015; Sarria et al., 2018; Wang et al., 2017; Wu, 2010).

Genetic defects leading to dysfunction or degeneration of photoreceptors cause vision impairment in retinal disorders such as age-related macular degeneration, retinitis pigmentosa, Leber congenital amaurosis and congenital stationary night blindness (Rattner et al., 1999). Studies in mouse models have shown that even before obvious cellular loss during the course of retinal disease, there may be structural and functional miswiring of the retinal circuits through a process of deafferentation (D'Orazi et al., 2014; Jones and Marc, 2005; Jones et al., 2012). In some disease models, the combination of abnormal photoreceptor synaptic signaling and photoreceptor loss induces exploratory dendritic behavior in BCs, resulting in the formation of aberrant synapses with novel synaptic partners [e.g. rod bipolar cell (RBCs) with cone photoreceptor] or at ectopic locations such as the ONL (Haverkamp, 2006; Jones and Marc, 2005; Jones et al., 2012; Peng et al., 2000; Soto and Kerschensteiner, 2015). The effectiveness of therapeutic interventions such as gene and cellular therapy depends on the ability of photoreceptors to reestablish appropriate synaptic connections (Gasparini et al., 2019; Singh et al., 2020). A better understanding of the mechanisms of synapse formation, specificity and maintenance at the OPL during human retinal development may provide insights into this synaptic plasticity.

Study of human fetal retina over the last 50 years has provided important insights into retinal and foveal development at molecular, cellular and functional levels (Cowan et al., 2020; Hendrickson and Drucker, 1992; Hendrickson and Zhang, 2019; Hendrickson et al., 2012; Hoshino et al., 2017; Ratnapriya et al., 2019; Sridhar et al., 2020). However, with restricted access to fetal tissue and an increasing need to complement animal models, human retinal organoids (HROs) derived from pluripotent stem cells have the potential to serve as a model system for human retinal development (O'Hara-Wright and Gonzalez-Cordero, 2020) and disease pathogenesis (Huang et al., 2019; Kruczek et al., 2021; Lukovic et al., 2020; Meyer et al., 2011; Parfitt et al., 2016). These three-dimensional structures may be produced through a variety of methods (Kuwahara et al., 2015; Zhong et al., 2014), yet all share the ability to mimic key aspects of retinal morphogenesis, including laminar organization of the major retinal cell types. Although others have described the development of photoreceptors and BCs in HROs (Capowski et al., 2019; Cowan et al., 2020; Hallam et al., 2018; Huang et al., 2019; Nakano et al., 2012) as well as the presence of ribbon synapse proteins at the OPL (Capowski et al., 2019; Cowan et al., 2020; Wahlin et al., 2017), it remains unknown

[1]Department of Surgery, The Vision Center, Children's Hospital Los Angeles, Los Angeles, CA 90027, USA. [2]The Saban Research Institute, Children's Hospital Los Angeles, Los Angeles, CA 90027, USA. [3]Core Center of Excellence in Nano Imaging, USC Michelson Center for Convergent Bioscience, University of Southern California, Los Angeles, CA 90089, USA. [4]Maternal-Fetal Medicine Division, Department of Obstetrics and Gynecology, Keck School of Medicine, University of Southern California, Los Angeles, CA 90033, USA. [5]Department of Ophthalmology, Roski Eye Institute, Keck School of Medicine, University of Southern California, Los Angeles, CA 90033, USA. [6]Department of Biochemistry and Molecular Medicine, Keck School of Medicine, University of Southern California, Los Angeles, CA 90033, USA. [7]Norris Comprehensive Cancer Center, Keck School of Medicine, University of Southern California, Los Angeles, CA 90033, USA.

*Author for correspondence (anagiel@chla.usc.edu)

S.P.B., 0000-0002-5830-8273; G.E.F., 0000-0002-8393-9229; D.C., 0000-0002-4478-2417; J.G.A., 0000-0002-6442-3032; A.N., 0000-0001-7275-6980

Handling Editor: Steve Wilson
Received 7 July 2021; Accepted 26 October 2021

Development (2021) 148, dev199551. doi:10.1242/dev.199551

to what extent HROs can serve as a model for OPL synaptogenesis and plasticity in the human retina and central nervous system.

In this study, we define stages of human OPL development in fetal retina based on cell morphogenesis and validate them by quantitative assessment of synaptic protein localization to the OPL. We then demonstrate that HROs recapitulate important features of outer retinal development and photoreceptor-bipolar cell synaptogenesis.

RESULTS

Staging of early OPL development in the human fetal retina

The formation of the OPL, defined as the nucleus-free neuropil between the ONL and INL, is dependent upon the spatial organization and maturation of photoreceptors, BCs, HCs and their respective synaptic endings. Before evaluating HROs as a model for OPL development, we sought to characterize OPL formation in the human fetal retina. The developing human retina displays a central to peripheral gradient of differentiation, which permits the study of a continuum of maturation in a single retinal section (Hendrickson, 2016). Owing to the limited availability of human fetal tissue at mid-gestation and beyond, our immunofluorescence analysis was performed on three fetal retinae obtained at fetal week 16.5 (~day 117), 16.6 (~day 118), and 19 (~day 133), which featured robust nuclear lamination centrally and an immature neuroblastic layer peripherally.

Based on the morphology and spatial organization of photoreceptors, BCs and HCs, we identified five distinct stages of OPL formation and show representative images from fetal week 16.6 retina (Fig. 1; Figs S1 and S2). The earliest stage, OPL-Stage 0, was located in the peripheral retina (Fig. 1A-D; Fig. S1A-D) and the most differentiated, OPL-Stage 4, was in the nascent fovea (Fig. 1Q-T; Figs S1Q-T and S2I-L) (Hendrickson, 2016). The detection of photoreceptors relied on the co-expression pattern of specific markers, namely RCVRN$^+$VSX2$^-$ (photoreceptor precursors), RXRγ$^+$ARR3$^-$ (immature cones), RXRγ$^+$ARR3$^+$ (maturing cones), NRL$^+$RHO$^-$ (immature rods) and NRL$^+$RHO$^+$ (maturing rods). Retinal interneurons were identified based on the expression of markers such as calbindin (CALB) and parvalbumin (PV; also known as PVALB) for HCs, PCP2 for depolarizing bipolar cells (DBCs), PKCα (PRKCA) for RBCs (a subset of DBCs), and PROX1 for HCs and BCs. VSX2 in combination with RCVRN was used to distinguish photoreceptor precursors (RCVRN$^+$VSX2$^-$) from other cell types in the presumptive INL (RCVRN$^-$VSX2$^+$) including neural retinal progenitors, BC precursors and BCs.

OPL-Stage 0 (Fig. 1A-D) is defined by the presence of photoreceptor precursors (RCVRN$^+$VSX2$^-$) spatially confined to the apical aspects of the neuroblastic layer, without a nucleus-free zone separating them from the rest of the cells (RCVRN$^-$VSX2$^+$) in the layer (Fig. 1A,B; Fig. S1A). HCs were present at the basal region of presumptive ONL of the neuroblastic layer (arrows, Fig. 1C, Fig. S1B; inset, Fig. S1B). Within the presumptive INL, the somata of DBCs (PCP2$^+$) were seen positioned along the apical aspect (arrows, Fig. 1C, Fig. S1B). The presumptive ONL also contained a single row of immature cones (RXRγ$^+$) at the most apical aspect, with two to three rows of immature rods (NRL$^+$) basal to the cone precursors (Fig. 1D).

In OPL-Stage 1 (Fig. 1E-H; Fig. S1E-H), a subtle separation between the nascent ONL and INL became apparent (arrowheads, Fig. 1E, Fig. S1E). The HC cell bodies were present at the interface between the nascent ONL and INL and aligned in a row apical to the DBCs, with short arbors directed toward the nascent ONL (arrowhead, Fig. 1F, Fig. S1F; inset, Fig. S1F). The DBCs at this stage bore unbranched dendrites extending to the apical surface of the nascent ONL (arrowhead, Fig. 1F) and basal axons extending toward the ganglion cell layer (GCL). The immature photoreceptors in OPL-Stage 1 lacked ARR3 and RHO expression (Fig. 1G,H).

In OPL-Stage 2 (Fig. 1I-L; Fig. S1I-L, Fig. S2A-D), an interrupted gap appeared between the ONL and INL (arrowheads, Fig. 1I, Fig. S1I, Fig. S2A) with short lateral extensions of HC processes (arrowheads, Fig. 1J, Fig. S1J; inset, Fig. S1J) and branching DBCs dendrites (arrowheads, Fig. 1J, Fig. S2B; inset, Fig. S2B) becoming confined to the nascent OPL. The axon terminals of DBCs extended to the IPL, with some axons traversing the GCL (Fig. 1J). Beginning at this stage onwards, PROX1$^+$ HCs and BC precursors became confined to the INL (Fig. S1D,H,L,P,T), notably including a single row of HCs along the apical aspect of the INL (arrows, Fig. S1L,P,T). The photoreceptor layer contained a laminar organization of immature rods and cones (Fig. 1K,L). RBCs with low expression of PKCα were first detected at this stage as a subset of PCP$^+$ DBCs (arrow, Fig. S2B-D).

At OPL-Stage 3, a continuous nucleus-free gap between the ONL and INL became identifiable (arrowheads, Fig. 1M, Figs S1M and S2E). The CALB$^+$ HCs were spaced apart with processes coursing along the OPL (arrowheads, Fig. 1N, Fig. S1N; inset, Fig. S1N); CALB$^+$ HCs represented a subset of PV$^+$ HCs (arrows, Fig. S1C,G, K,O,S,T). Branched DBC dendrites were restricted to the OPL (arrowheads, Fig. 1N, Fig. S2F; inset, Fig. S2F) and most of the DBC axons terminated in the IPL (Fig. 1N). The photoreceptor nuclei were arranged in two sub-layers: an apical row of cones (RXRγ$^+$; Fig. 1O), including some expressing ARR3 at low levels (arrow, Fig. 1P), and rows of rods (NRL$^+$; Fig. 1O). PKCα-expressing RBCs (arrows, Fig. S2G,H) were present even though the rods remained immature at fetal week 16.6 (RHO$^-$; Fig. 1P).

OPL-Stage 4 was identified in the most central region and represented nascent fovea in fetal week 16.6 retina (Fig. 1Q-T; Fig. S1Q-T, Fig. S2I-L), with a prominent nucleus-free gap (arrowheads, Fig. 1Q, Figs S1Q and S2I) and a distinct one cell-thick row of HCs constituting an apical layer in the INL (arrows, Fig. 1Q,R, Figs S1Q,S,T and S2I). The CALB$^+$ HCs formed a thick dendritic plexus along the OPL (arrowheads, Fig. 1R, Fig. S1R; inset, Fig. S1R). The branched DBC neurites were confined to the OPL (arrowheads, Fig. 1R, Fig. S2J; inset, Fig. S2J) and IPL and their cell bodies were spaced apart (arrow, Fig. S2J). A single row of maturing RXRγ$^+$ARR3$^+$ cones constituted the ONL with a notable absence of rods (Fig. 1S,T) and RBCs (Fig. S2K). Of note, in fetal week 19 retina, OPL-Stage 4 was identified in parafoveal sections which contained RHO$^+$ rods and PKCα$^+$ RBCs. Because human fetal retina older than 19 weeks was not available, it remains unclear to what extent these OPL-Stage 4 features relate to foveal versus parafoveal anatomical specializations.

Thus, through systematic evaluation of laminar arrangement, cell morphology and maturation state, we have identified early stages of human OPL development in pseudo-time using three human fetal retinae. A useful aspect of this staging system is that the nuclear arrangement of PRs, HCs and BCs alone correlated with stage, and therefore the nuclear lamination pattern can be used to identify regions belonging to each OPL stage.

Stage-specific subcellular localization of synaptic proteins in the human fetal retina

During retinal development, the maturation of photoreceptors and BCs is accompanied by trafficking of synapse proteins to their terminals at the OPL (Regus-Leidig et al., 2009). We analyzed the spatial location of synapse proteins at each stage of OPL

Development (2021) 148, dev199551. doi:10.1242/dev.199551

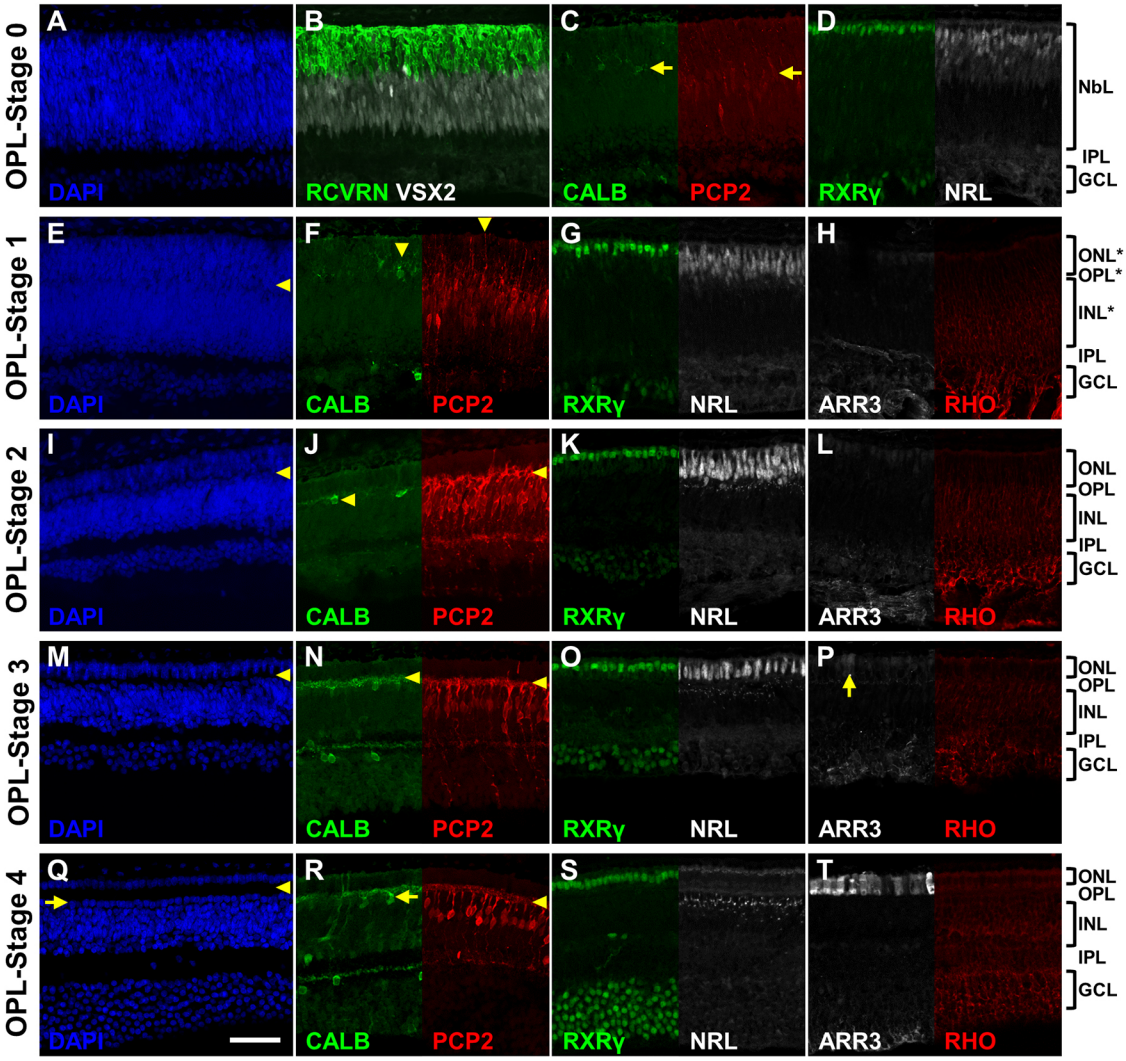

Fig. 1. Staging of OPL development in human fetal retina. (A-T) Representative immunofluorescence images of a fetal week 16.6 (~D118) retina showing cellular morphogenesis at OPL-Stage 0 (A-D), OPL-Stage 1 (E-H), OPL-Stage 2 (I-L), OPL-Stage 3 (M-P) and OPL-Stage 4 (Q-T). Cell-type specific markers were used in combination to identify photoreceptor precursors (RCVRN^{+}VSX2^{-} in B; RXRγ^{+} and NRL^{+} in D,G,K,O,S), non-photoreceptor cells (RCVRN^{-}VSX2^{+} in B), HCs (CALB^{+} in C,F,J,N,R), DBCs (PCP2^{+} in C,F,J,N,R), maturing cones (ARR3^{+} in H,L,P,T) and maturing rods (RHO^{+} in H,L,P,T). Of note, a subset of RGCs in the GCL (F,N,R), amacrine cells in the INL (R) and Müller glia in the INL (R) expressed CALB. RXRγ expression is also detected in RGCs in the GCL (D,G,K,O,S). Stage-specific features are pointed out with yellow arrows and arrowheads. Arrows: spatial location of nascent HCs and DBCs (C); a single row of HCs (Q); maturing cones beginning to express ARR3 (P). Arrowheads: developing OPL (E,I,M,Q); HC processes and DBC dendrites (F,J,N,R). Asterisks indicate nascent layers in OPL-Stage 1. Scale bar: 50 µm (A-T).

development in human fetal retinae, including the presynaptic proteins bassoon (BSN) and ribeye (CTBP2) (Fig. 2) and the postsynaptic receptor mGluR6 (GRM6) (Fig. 3). The pattern of nuclear arrangement guided the identification of regions belonging to the five OPL stages on consecutive sections derived from the same fetal week retinae analyzed in Fig. 1, and we show representative images from fetal week 16.6 retina.

In OPL-Stage 0 (Fig. 2A-D) and OPL-Stage 1 (Fig. 2E-H), bassoon and ribeye puncta were found dispersed in the neuroblastic layer. By OPL-Stage 2 (Fig. 2I-L), bassoon and ribeye began to localize within the developing OPL. In OPL-Stage 3 (Fig. 2M-P) and OPL-Stage 4 (Fig. 2Q-T), the bassoon and ribeye aggregates were limited to a narrow band along the photoreceptor terminals. Across all stages, bassoon and ribeye puncta were colocalized (Fig. 2D,H,L,P,T). We quantified bassoon puncta location in the three fetal retinae using a semi-automated fluorescence intensity detection method (see supplementary Materials and Methods; Fig. 2U; Fig. S3). This revealed a drastic decrease in interquartile range (IQR) values for puncta intensity density distributions from OPL-Stage 1 to OPL-Stage 3 (Fig. 2U). This was also depicted as narrowing of the peaks at the median, which represents the OPL (Fig. S3A). Taken together, the change in bassoon puncta localization from OPL-Stage 0 to OPL-Stage 4 across three retinae was statistically significant (P<0.0001, omnibus F-test). Pair-wise comparison of OPL stages within each fetal retina was performed based on bassoon intensity density IQR values using restricted maximum likelihood models (Fig. S3B). The IQR values of OPL-Stage 0 versus OPL-Stage 1 and OPL-Stage 3 versus OPL-Stage 4 were not significantly different, whereas OPL-Stage 0 or 1 versus OPL-Stage 2 or 3 or 4 were significant after multiple test corrections (P<0.001, adjusted significance cut-off). This finding shows that the major changes in bassoon and ribeye synaptic localization are occurring from OPL stages 1 to 3.

Development (2021) 148, dev199551. doi:10.1242/dev.199551

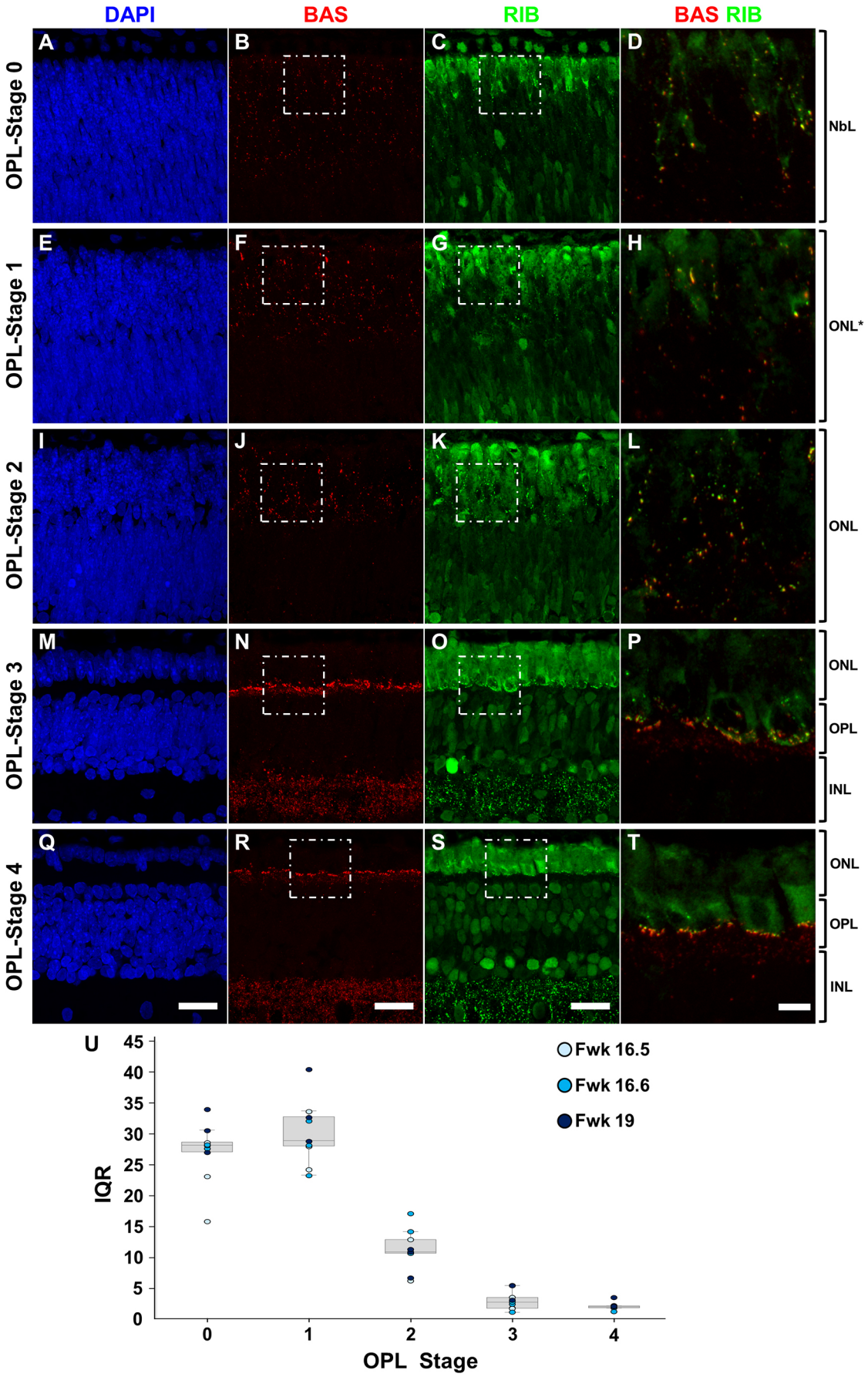

Fig. 2. See next page for legend.

Development (2021) 148, dev199551. doi:10.1242/dev.199551

Fig. 2. Spatial distribution of presynaptic ribbon proteins by OPL stage in human fetal retina. (A-T) Representative immunofluorescence images of a fetal week 16.6 (~D118) retina revealing synaptic localization of bassoon and ribeye to the OPL along five OPL stages: OPL-Stage 0 (A-D), OPL-Stage 1 (E-H), OPL-Stage 2 (I-L) OPL-Stage 3 (M-P) and OPL-Stage 4 (Q-T). In addition to ribeye, the anti-CtBP2 antibody detects C-terminal-binding protein 2 (CtBP2, nuclear staining in ONL and INL in C,G,K,O,S of the ribeye panel). The expression of ribeye was distinguished from nuclear staining based on punctate staining. Boxed regions on bassoon (B,F,J,N,R) and ribeye (C,G,K,O, S) panels are shown at higher magnification in D,H,L,P,T with layer labels on the right corresponding only to these magnified insets (asterisk indicates nascent ONL). Bassoon (N,R) and ribeye (O,S) puncta in the IPL can be seen at the basal aspect of the INL in OPL-Stage 3 and OPL-Stage 4 images. (U) Bassoon puncta intensity density distribution along the apical-basal axis in a volume of 30 µm×60 µm×2.01 µm, represented as a boxplot with individual IQR values plotted by stage from three retinae. Boxplot shows median values (middle bars), and first to third interquartile ranges (boxes); whiskers indicate 1.5 times the interquartile range; dots represent individual ROIs (color-coded according to key). *n*=3 ROI analyzed per stage per retina, except for fetal week 16.5 which lacked sections corresponding to OPL-Stage 4. Scale bars: 20 µm (A-C,E-G,I-K,M-O,Q-S); 5 µm (D,H,L,P,T).

mGluR6, the postsynaptic glutamate receptor of DBCs, was detected in both photoreceptors and BCs (Fig. 3). The mGluR6 antibody initially stained the entire nascent photoreceptor cell membrane (Fig. 3C,G) with increasing immunoreactivity at the apical and basal membranes (Fig. 3K,O). There is evidence for photoreceptor expression of mGluR6 from single-cell transcriptomic analysis of developing mouse retina (Clark et al., 2019) and immunofluorescence performed on fetal week 24 human retina (Hendrickson and Zhang, 2019). Punctate mGluR6 expression in DBCs showed increasing localization to the OPL through OPL-Stage 2 (Fig. 3K,L) and OPL-Stage 3 (Fig. 3O,P), culminating in a narrow band by OPL-Stage 4 (Fig. 3S,T) that was apposed to presynaptic bassoon (arrowheads, Fig. 3P,T). The synaptic localization of bassoon and ribeye preceded that of mGluR6.

In summary, human OPL developmental stages are accompanied by quantifiable changes in presynaptic protein localization and corresponding postsynaptic protein expression at the synapse. The stage-specific features are summarized in Fig. 4.

Time course of OPL formation in cultured HROs

Having characterized early OPL development in the human fetal retina, we next sought to ascertain the time course of OPL formation in HROs derived from two stem cell lines: the human induced pluripotent stem cell (iPSC) line WTC11 (Fig. 5) and the human embryonic stem cell (ESC) line H9 (Fig. S4). In HROs, OPL formation was defined by the emergence of a nucleus-free zone between ONL and INL, accompanied by the spatial organization of photoreceptors, BCs and HCs. We analyzed HROs generated by the Zhong et al. protocol (Zhong et al., 2014) (Fig. 5A) sampled every 60 days from day (D) 100 in culture (D100) to D280 (Fig. 5B-E; Fig. S4A-P).

Based on the HRO staging criteria proposed by Capowski et al. (2019), our HROs were at stage 2 by D100 and were at stage 3 in all subsequent ages (Fig. 5F-M; Fig. S4E-P). At D100, HROs contained a neuroblastic layer composed of immature cells, with photoreceptor precursors (RXRγ$^+$ARR3$^-$ cones and NRL$^+$RHO$^-$ rods) confined to the apical aspect and a few DBCs (PCP2$^+$) on the basal aspect (Fig. 5F,G; Fig. S4E-G). By D160, a distinct ONL and OPL were identifiable, with maturing photoreceptors (ARR3$^+$ cones and RHO$^+$ rods) and interneurons (PCP2$^+$ DBCs, CALB$^+$ HCs, PKCα$^+$ RBCs) separated by a nucleus-free zone (Fig. 5H,I; Fig. S4H-J). The subsequent ages, at D220 and D280 (Fig. 5J-M; Fig. S4K-P), demonstrated further maturation of the ONL, OPL and INL. In general D220 HROs bore longer apical structures (Fig. 5D; Fig. S4C), a wider OPL (Fig. 5J,K; Fig. S4K-M), more HC lateral processes through the OPL (Fig. 5J; Fig. S4M) and an increased number of RBCs (Fig. 5K; Fig. S4M). However, by D280 we observed no further improvement in these features (Fig. 5L,M; Fig. S4N-P), likely representing a plateau in HRO development that has been described by others (Cowan et al., 2020). This establishes a window from D100 to D160 in these iPSC- and ESC-derived HROs for laminar arrangement of photoreceptors in the ONL, and DBCs and HCs in the INL, with further maturation of these cell types during the D160 to D220 time period. Because the WTC11 iPSC-derived and H9 ESC-derived organoids appeared comparable, we subsequently describe in detail findings from WTC11 HROs unless otherwise specified.

Inter- and intra-organoid variability in the HRO model system

In the absence of external developmental gradients, the self-patterned retinal organoids have been reported to exhibit extensive inter- and intra-organoid variability (Browne et al., 2017; Capowski et al., 2019; Phillips et al., 2018). Consistent with previous reports, based on the light-microscopic features of HROs developing from iPSC aggregates, we observed a variable pace of retinal induction within and between multiple HRO preparations from H9 (*n*=10) and WTC11 (*n*=10) cell lines. To characterize regional variations within HROs that appear similar under light microscopy [stage 3 per Capowski et al. (2019)], we analyzed the architecture and maturation of photoreceptors, HCs and DBCs, and localization of bassoon and ribeye in D160 HROs (Fig. 6; Fig. S5). Sections of distinct HROs from the same preparation revealed regions with distinct cellular compositions and maturation states, as for example in HRO 1 versus HRO 2 in Fig. 6A-A′ and Fig. S5A-D′. Whereas HRO 1 contained regions with varying densities of ARR3$^+$ cones and PCP2$^+$ DBCs, HRO 2 had a more uniform distribution of these cell types (Fig. 6A).

Not only was there variability between organoids but also within individual organoids, as exemplified by regions of interest (ROI) 1 and 2 in Fig. 6A,A′ and Fig. S5A-D′. These regions were within the same HRO and had similar cellular density (Fig. 6B,B′) yet: (1) maturing ARR3$^+$ cones were more abundant in ROI 2 (Fig. 6C,C′); (2) maturing RHO$^+$ rods were more abundant in ROI 2 (Fig. 6D′), but almost absent in ROI 1 (Fig. 6D) despite similar numbers of immature NRL$^+$ rods; (3) ROI 1 and ROI 2 differed in the density of DBCs (Fig. 6F,F′) and RBCs (Fig. 6G,G′); (4) ROI 1 contained well-organized CALB$^+$ HCs (Fig. 6E) compared with ROI 2 (Fig. 6E′); and (5) the photoreceptor ribbon synapse proteins bassoon (Fig. 6H) and ribeye (Fig. 6I) showed better confinement along the OPL in ROI 1 (Fig. 6H′,I′). Inter- and intra-organoid variability in maturation state of retinal cell types was quantified on four arbitrary ROIs per HRO (total ROIs analyzed=24) from three independent differentiation experiments (detailed description in supplementary Materials and Methods). We found significant variation between organoid regions within a single organoid (P=0.01) and between organoids (P=0.005). In addition to the variability in maturation state and numbers by cell type, we also observed a lack of synchrony in the maturation states of adjacent photoreceptors, HCs and DBCs. For example, ROI 1 demonstrates more mature HCs adjacent to immature rods and sparse cones (Fig. 6D,E) compared with robust rod maturation and abundant cones in ROI 2 adjacent to immature/absent HCs (Fig. 6D′,E′).

Differences in cellular composition and maturation state were observed in every organoid age across five independent HRO

Development (2021) 148, dev199551. doi:10.1242/dev.199551

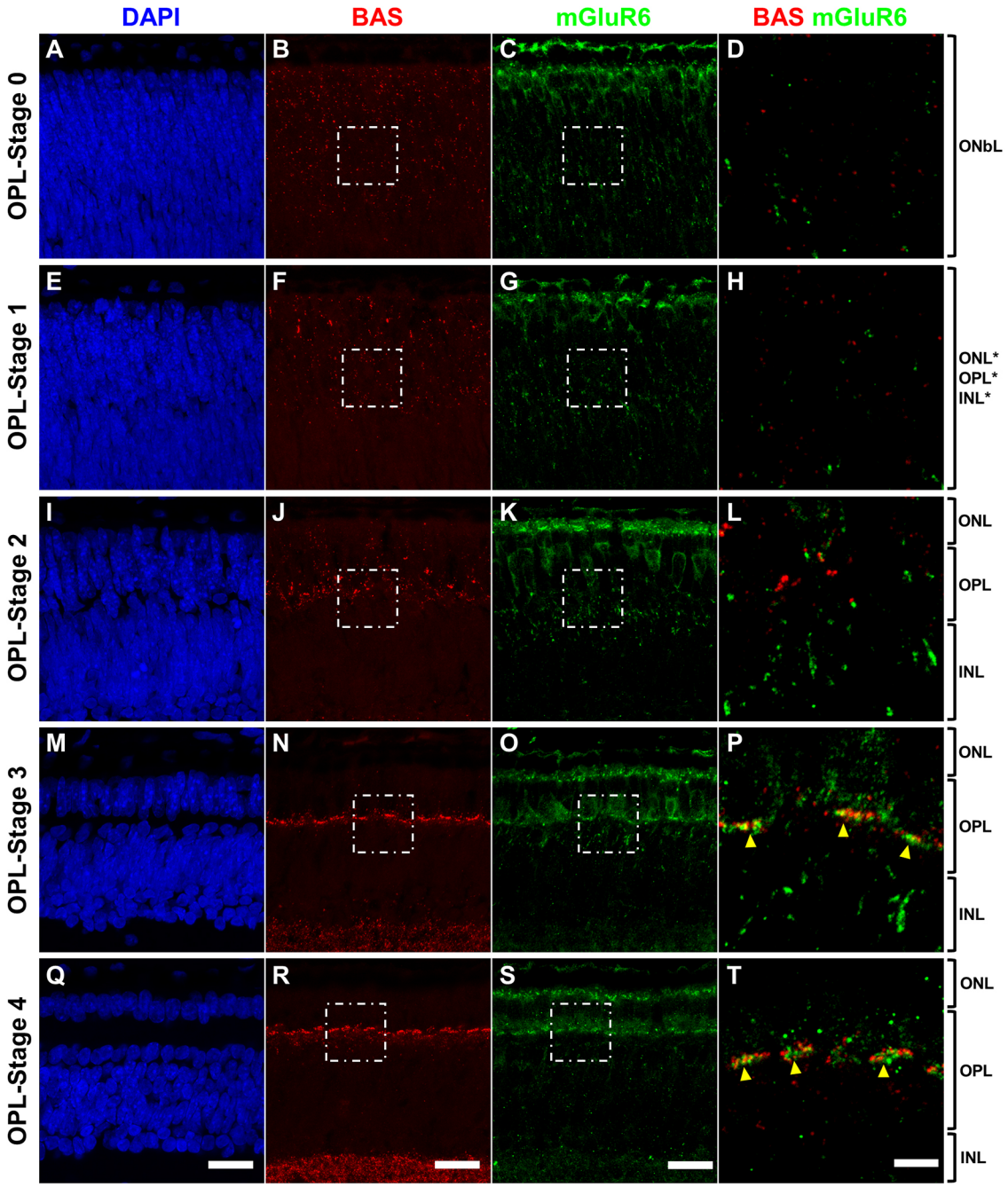

Fig. 3. Spatial distribution of presynaptic bassoon and postsynaptic mGluR6 by OPL stage in human fetal retina. (A-T) Representative immunofluorescence images of a fetal week 16.6 (~D118) retina showing bassoon and mGluR6 at five OPL stages: OPL-Stage 0 (A-D), OPL-Stage 1 (E-H), OPL-Stage 2 (I-L), OPL-Stage 3 (M-P) and OPL-Stage 4 (Q-T). Boxed regions on bassoon (B,F,J,N,R) and mGluR6 (C,G,K,O,S) panels are shown at higher magnification in D,H,L,P,T. Yellow arrowheads point out aggregation of bassoon and mGluR6 at the OPL (P,T). Asterisks indicate nascent layers. Scale bars: 20 µm (A-C,E-G,I-K,M-O,Q-S); 5 µm (D,H,L,P,T).

preparations. This inter- and intra-organoid variability and dyssynchrony in the development of adjacent cell types made it difficult to designate ROI to a single OPL stage (Figs 1 to 4; Figs S1 and S2). This led us to apply OPL staging criteria to individual cell types or features during HRO maturation.

Recapitulation of OPL morphogenesis in HROs

OPL morphogenesis in HROs was studied using immunofluorescence on fixed sections from D100 to D220 (Figs 7 and 8). PRs, BCs and HCs were compared with human fetal retina, based on the OPL staging criteria described in Fig. 1 and Fig. 4, with emphasis on the kinetics of photoreceptor marker expression (Fig. 7) and neurite morphology of DBCs and HCs (Fig. 8). The most mature feature of each cell type was chosen to represent the developmental state of the respective HROs (Figs 7 and 8). In order to validate cell type-specific markers, staining of CALB, SNCG, ONECUT1, BRN3 and RXRγ was performed on retina at fetal week 16.6 and HROs from D70 to D280 (Fig. S6).

Based on the temporal expression pattern of photoreceptor cell-type specific markers, organoid cones and rods were found to mimic

Development (2021) 148, dev199551. doi:10.1242/dev.199551

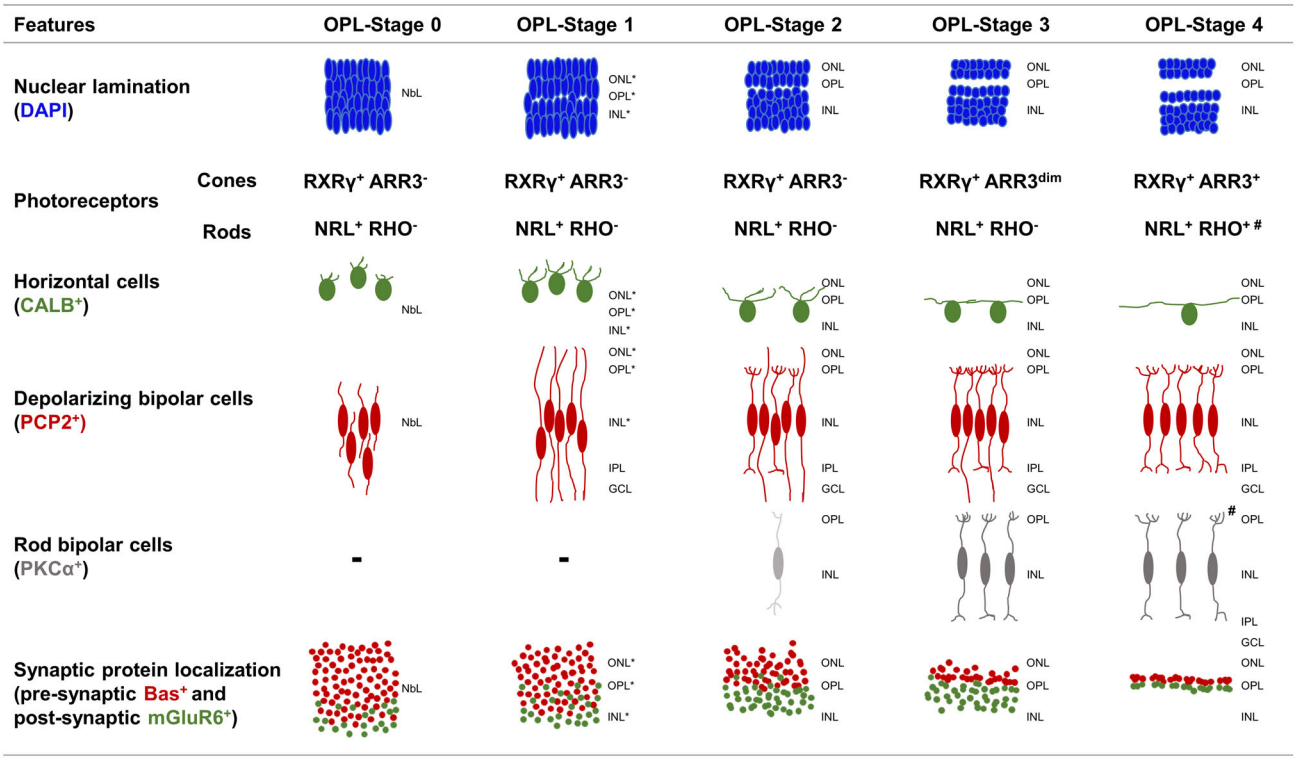

Fig. 4. Summary schematic of stage-specific features of OPL morphogenesis and synaptic protein localization in mid-gestational human fetal retina. The pseudo-temporal developmental events in photoreceptors, HCs, DBCs and RBCs in human fetal retina along OPL-Stages 0 to 4 are depicted. Nuclear lamination: beginning with a single neuroblastic layer in OPL-Stage 0, a nuclear gap emerges and widens by OPL-Stage 4. Photoreceptors: cone precursors (RXRγ$^+$) begin to express ARR3 by OPL-Stage 3 with robust staining in the nascent fovea (OPL-Stage 4). NRL$^+$ rod precursors remain RHO$^-$ in OPL-Stage 3 at fetal week 16.6, but begin to express RHO in OPL-Stage 4 at fetal week 19. Horizontal cells: initially found at the basal aspect of the presumptive ONL (OPL-Stage 0), the HCs then exist as a single layer along the apical portion of the INL (OPL-Stage 2) with long dendrites extending within the OPL (OPL-Stage 3 and 4). Depolarizing bipolar cells (DBCs): At OPL-Stage 1, the DBCs have dendrites extended into the apical aspect of nascent ONL which subsequently branch strictly within the OPL (OPL-Stage 3 and 4). Rod bipolar cells: PKCα$^+$ RBCs are first evident at OPL-Stage 2. RBCs are absent from nascent fovea in fetal week 16.6 and present in parafovea in fetal week 19 (OPL-Stage 4). Synaptic proteins: bassoon and mGluR6 are expressed early in the presumptive ONL and INL of the neuroblastic layer respectively (OPL-Stage 0). Bassoon and mGluR6 become confined to the OPL by OPL-Stage 3 and OPL-Stage 4, respectively, culminating in their apposition at the OPL. Asterisks indicate nascent layers. # indicates rod and RBC features specific to the parafoveal retina in the older fetal week 19 retina.

the fetal developmental trajectory (Fig. 7A) by traversing through OPL-Stages 0 to 4 (Fig. 7B-I). Cones matured from RXRγ$^+$ARR3$^-$ (inset, Fig. 7B) to RXRγ$^+$ARR3$^+$ (insets, Fig. 7D,E,F,H), and rods went from NRL$^+$RHO$^-$ (inset, Fig. 7C) to NRL$^+$RHO$^+$ (insets, Fig. 7D,E,G,I). Interestingly, organoid cones demonstrated maturation beyond OPL-Stage 4 as further evidenced by the presence of apical inner segments and basal pedicles in the cones (insets, Fig. 7E,F,H). Based on morphology alone, these HRO cones (insets, Fig. 7E,F,H) resemble cones in mid-peripheral retina at fetal week 26 (Hendrickson and Drucker, 1992).

PCP$^+$ DBCs also developed from OPL-Stage 0 to 3 during a span from D100 to D160 (Fig. 8A-D′). DBCs were evident in HROs at D100 (Fig. 8B) and subsequently demonstrated cell body restriction to the INL with dendritic extensions into the ONL (arrowhead, Fig. 8C). As in fetal retina, these DBC dendrites became confined to the OPL (Fig. 8D) by OPL-Stage 3, and a subset of cells expressed the RBC marker PKCα (arrow, Fig. 8D′). It should be noted that significant loss of retinal ganglion cells (RGCs) in HROs during the time period of our study (Fig. S6D,F, H,J,L,M) precluded analysis of DBC maturation with respect to their basal axons.

Staining for CALB allowed us to visualize HC processes as they extended into the OPL along OPL-Stages 0 to 3 in HROs (Fig. 8E-I′). In regions that lacked a distinct OPL, we observed HCs with short processes (arrow, Fig. 8F,F′), but as the HCs extended their processes laterally, a distinct OPL became more evident (arrows, Fig. 8G-H′). HC processes were found to extend further as they approached D220 (arrow, Fig. 8I,I′), but in general formed a thinner plexus compared with that seen in OPL-Stage 3 fetal retina (Fig. 1N; Fig. S1N).

In summary, detailed analysis of the cell types contributing to OPL formation – the photoreceptors, BCs and HCs – reveals a remarkable recapitulation of this process in HROs beyond OPL-Stage 4 in photoreceptors and through OPL-Stage 3 for BCs and HCs.

Bassoon and ribeye localization to the OPL in HROs

We next examined whether HROs mimic the localization of synaptic proteins to the OPL observed in fetal retina (Fig. 9; Fig. S7, Fig. S8). Analysis of HRO sections at ages D70, D100, D145 and D160 revealed subcellular trafficking of bassoon to the OPL in maturing photoreceptors (arrowheads, Fig. 9A-P). At D160, a precise localization of bassoon and ribeye puncta was observed at the OPL (Fig. 9Q,R), and these two presynaptic ribbon proteins were appositioned (Fig. 9R).

By staining WTC11 and H9 HROs (Fig. 10 and Fig. S7, respectively) for bassoon and ribeye from D100 to D220, we observed cotransport to the OPL localization in a fashion resembling OPL-Stages 0 to 3 (Fig. 10A-U; Fig. S7A-L). To confirm this, we manually quantified the spatial distribution of bassoon and ribeye puncta along the apical-basal (*y*) axis of WTC11 HRO regions per age

Development (2021) 148, dev199551. doi:10.1242/dev.199551

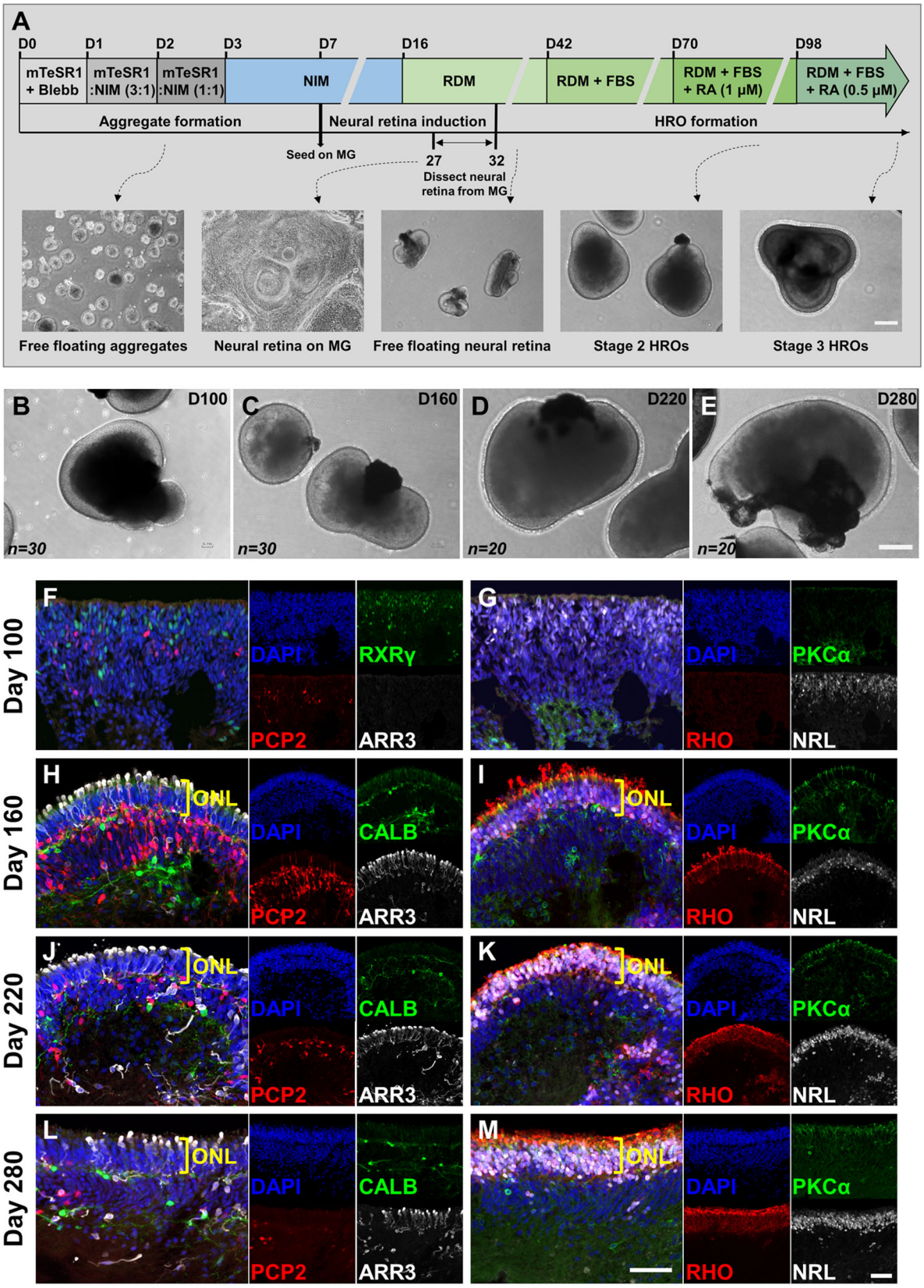

Fig. 5. OPL formation in WTC11 iPSC-derived human retinal organoids. (A) Schematic of HRO generation protocol (adapted from Zhong et al., 2014) used in this study. (B-E) Representative light microscopy images of live HROs at four ages: D100 (B), D160 (C), D220 (D) and D280 (E). *n*, number of HROs analyzed at each age from seven to ten independent HRO preparations. (F-M) Immunofluorescence staining of HROs at four ages for cone precursors (RXRγ^{+}ARR3^{-}; F), maturing cones (RXRγ^{+}ARR3^{+}; H,J,L), DBCs (PCP2^{+}; F,H,J,L), HCs (CALB^{+}; H,J,L), rod precursors (NRL^{+}RHO^{-}; G), maturing rods (NRL^{+}RHO^{+}; I,K,L) and RBCs (PKCα^{+}; I,K,M). Serial sections are shown at each age on the right and left panels. Yellow brackets in H-M indicate ONL. Blebb, blebbistatin; FBS, fetal bovine serum; MG, matrigel; NIM, neural induction medium; RA, retinoic acid; RDM, retinal differentiation medium. Scale bars: 300 µm (A-E); 50 µm (F-M).

Development (2021) 148, dev199551. doi:10.1242/dev.199551

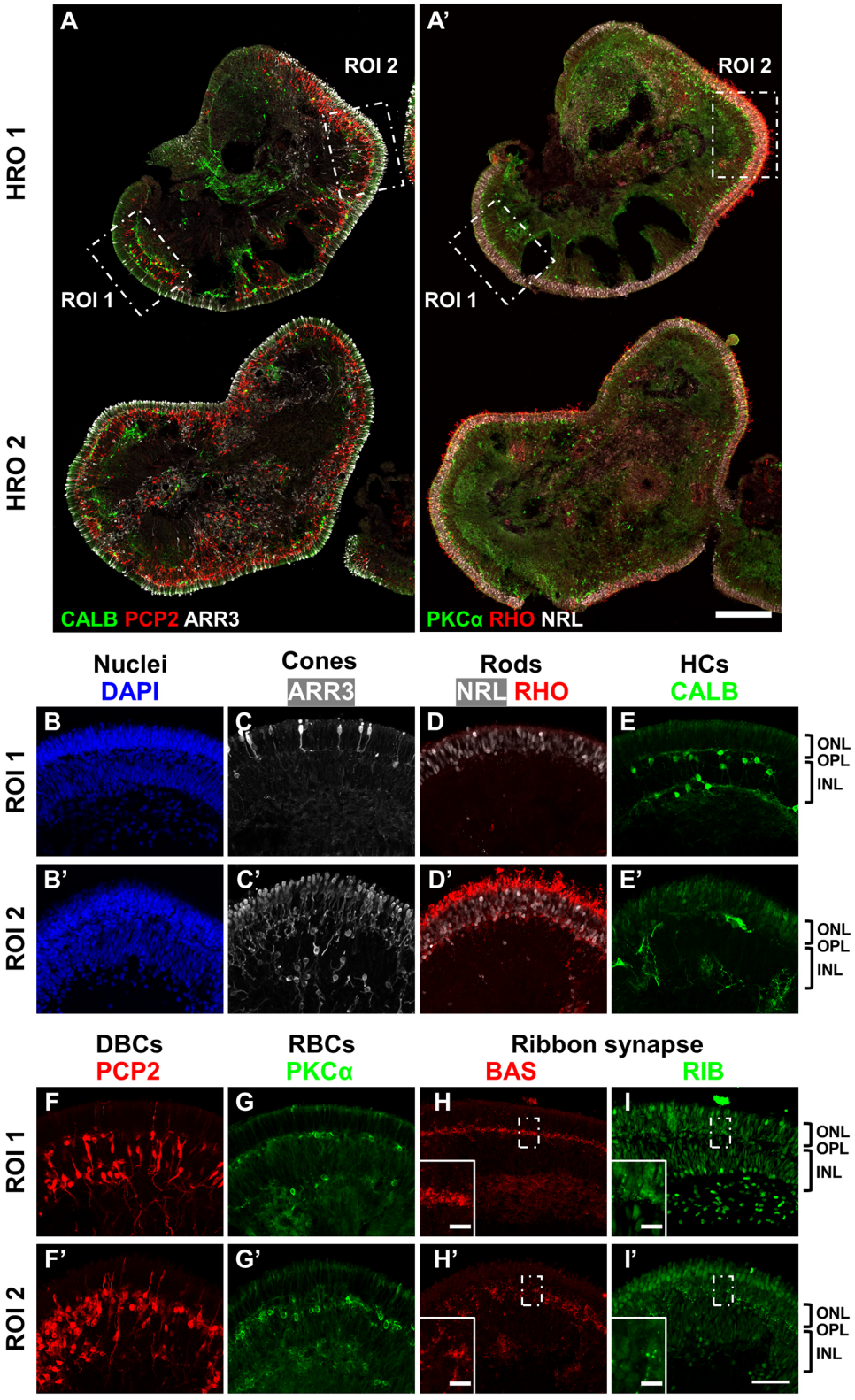

Fig. 6. Inter- and intra-organoid variability in cellular composition and maturational state. (A-I′) Representative immunofluorescence images of WTC11 iPSC-derived HROs at D160 showing variability in cell density, distribution and maturation state between each other (A-A′) and within a single HRO (B-I′). Boxed areas in A,A′ indicate selected regions of interest, ROI 1 and ROI 2, which are shown at higher magnification in B-I′. ROI 1 and ROI 2 demonstrate variations in OPL width (B,B′), cones (C,C′), rods (D,D′), HCs (E,E′), DBCs (F,F′), RBCs (G,G′), and bassoon (H,H′) and ribeye (I,I′) ribbon synapse proteins. Insets in H-I′ show magnified ROI. Scale bars: 200 µm (A,A′); 50 µm (B-I′); 10 µm (H-I′ insets).

on 4 µm-thick confocal volumes (see supplementary Materials and Methods; Fig. 10V). We observed a marked increase and narrowing of puncta count density peak most pronounced from D130 to D160 as quantified by IQR values (D100 to D220: $P<0.0001$, omnibus F-test; Fig. 10V). At D220, the puncta staining appeared to be similar to D160. The age-wise comparisons D100 or D130 versus D145 or D160 or D220 were significantly different after multiple test corrections ($P<0.001$, adjusted significance cut-off) for both proteins, whereas the rest of the comparisons were non-significant. These findings indicate that the most prominent change in bassoon and ribeye spatial distribution occurs from D130 to D145, with culmination of targeting by D160, and with no further refinement at D220.

Applying automated quantification of bassoon puncta fluorescence intensity, we confirmed a marked drop in IQR values from D130 to

Development (2021) 148, dev199551. doi:10.1242/dev.199551

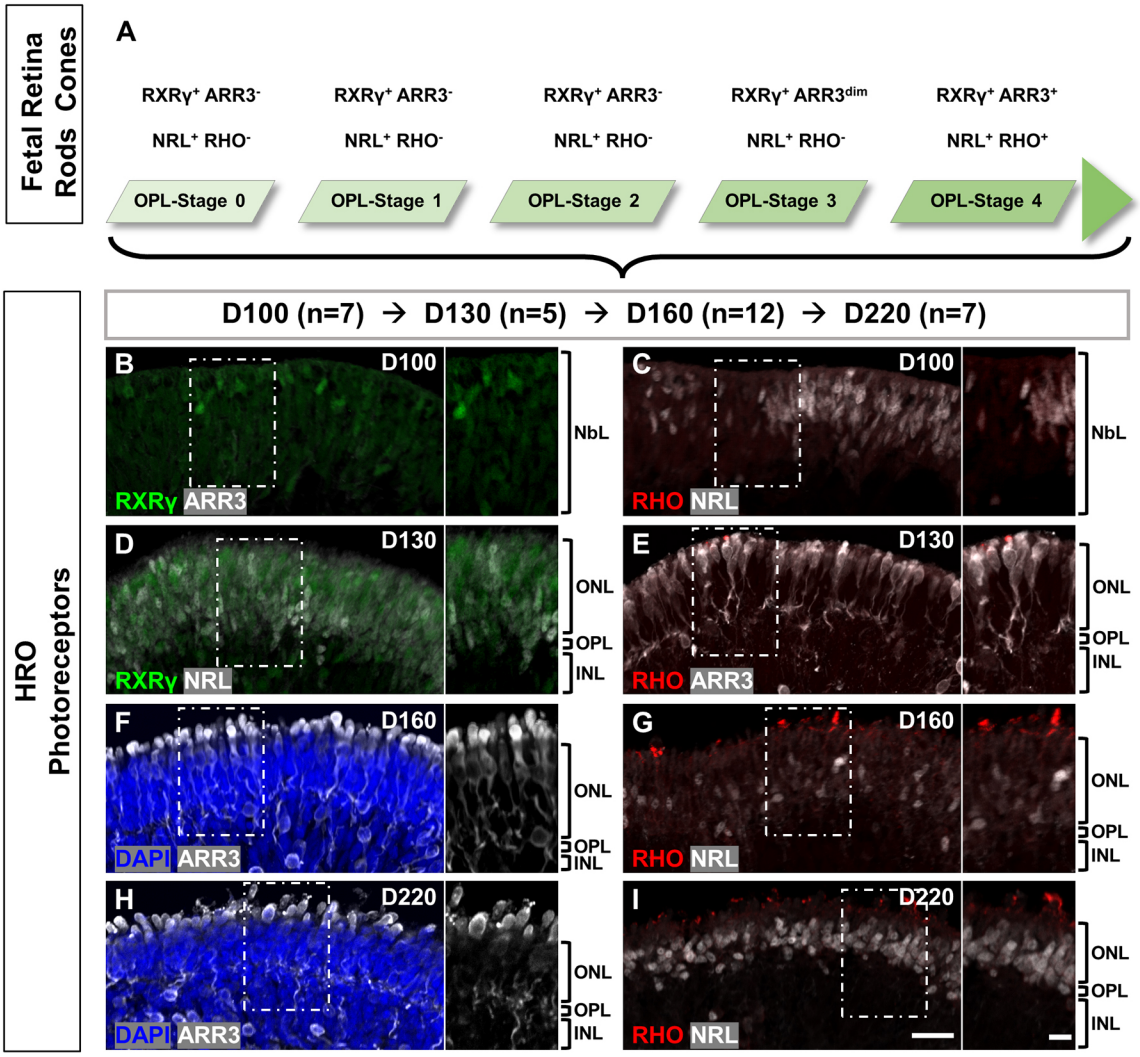

Fig. 7. Characterization of photoreceptors in WTC11 iPSC-derived HROs based on OPL stage-specific features. (A) Schematic showing characteristic features of human fetal retina photoreceptors at OPL stages 0 to 4 that are recapitulated by photoreceptors in HROs. (B-I) Representative immunofluorescence images of HROs at ages D100 to D220 showing nuclear lamination (B-I), marker expression pattern (B-I) and morphological maturation of photoreceptors (E-I). The boxes on B-I indicate selected ROI and insets show them magnified. *n*, number of HROs evaluated at each age. Scale bars: 50 µm.

D160 in HROs (P<0.0001, omnibus F-test; Fig. S8A,B) with a similar sigmoidal distribution as exhibited by fetal retina (Fig. 2U; Fig. S3A). Pair-wise comparison of HRO ages versus fetal retina OPL stages was performed in order to correlate the two developmental models (Fig. S8B). Using the higher P-value as an indicator of pairs with least difference between each other, in general we found that increasing HRO age correlated with increasing OPL stage (Fig. S8C). The pairwise comparisons indicated similarity between HROs at D100 to D130 with OPL-Stage 0 to 2, and D145 to D220 with OPL-Stage 2 to 4, confirming the ability of HROs to recapitulate a human fetal OPL development.

These results show robust presynaptic localization of ribbon proteins in HROs up to the equivalent of OPL-Stage 3 in human fetal retina (Fig. 10; Fig. S7). This finding establishes a quantitative framework for ascertaining the stage of OPL development in HRO regions.

Synapse assembly at the OPL in HROs

To determine whether bassoon and ribeye localization to the OPL coincided with photoreceptor-bipolar cell synapse assembly, we examined HROs for expression of the postsynaptic mGluR6 and the presynaptic L-type calcium channel protein $Ca_v1.4$. Certain regions of D160 HROs (Fig. 11A-F) contained mGluR6 puncta on dendrites of: (1) $PKC\alpha^+$ RBCs (arrowheads, Fig. 11B) in proximity to ribeye puncta (arrowheads, Fig. 11C), and (2) $PCP2^+$ DBCs (arrowheads, Fig. 11E) in proximity to cone pedicles (arrowheads, Fig. 11F). Transmission electron micrographs of D160 HROs (Fig. 11G) provide ultrastructural evidence of synaptic ribbons with tethered synaptic vesicles (arrowheads, Fig. 11H,I). At D220, we observed certain regions with punctate expression of $Ca_v1.4$ at the OPL (arrowheads, Fig. 11J-L). The expression of mGluR6 and $Ca_v1.4$ in HROs, in conjunction with the presence of ribbon structures and synaptic vesicles on electron microscopy, supports the possibility of functional synapses in HROs.

DISCUSSION

In this study we have staged human OPL development and found remarkable similarities between human fetal retina and retinal organoids. The main findings are that: human fetal retina develops through distinct stages with regard to OPL formation, characterized by nuclear lamination, molecular maturation of

Development (2021) 148, dev199551. doi:10.1242/dev.199551

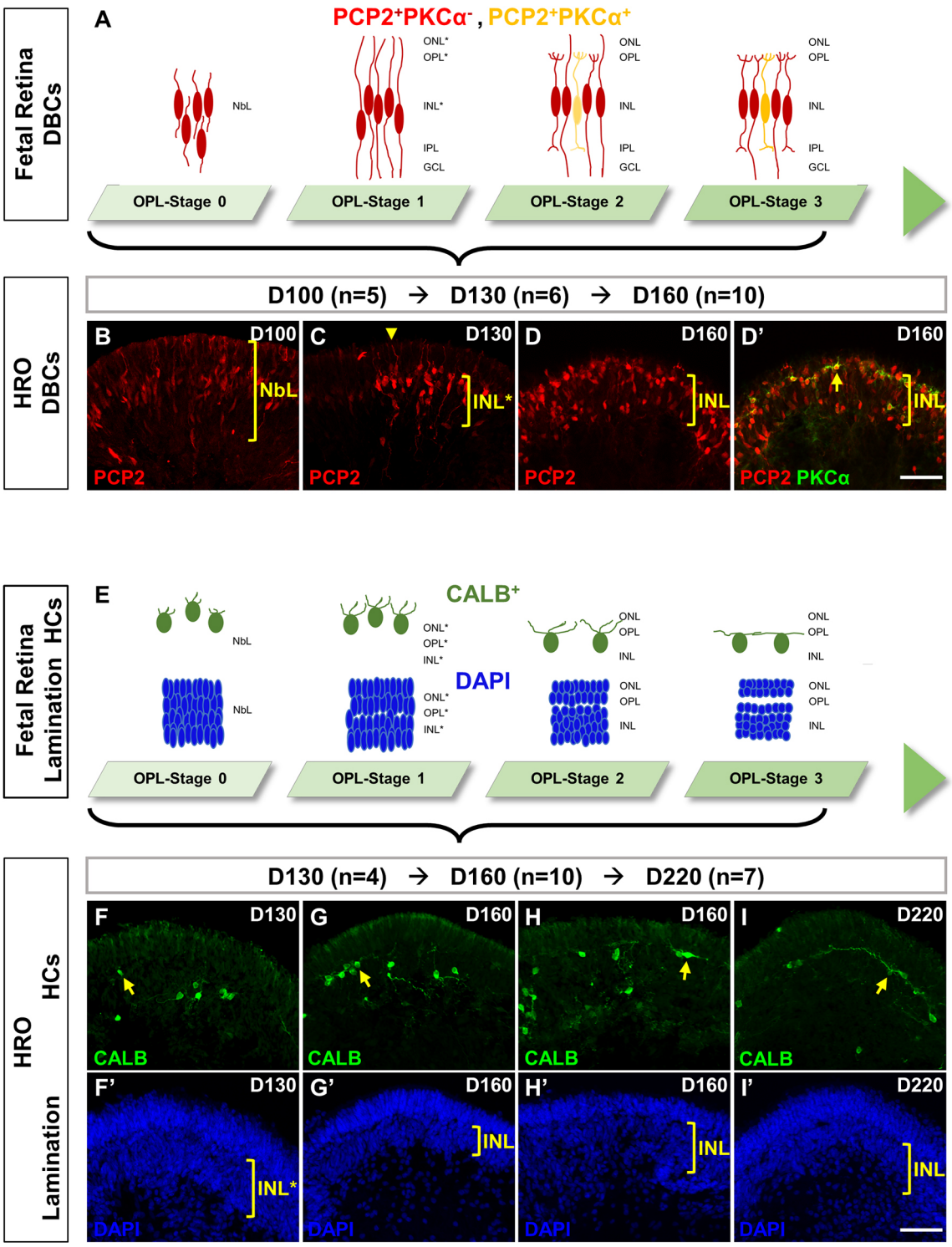

Fig. 8. Characterization of DBC and HC morphogenesis in WTC11 iPSC-derived HROs based on OPL stage-specific features. (A) Schematic showing characteristic features of DBCs recapitulated in HROs. (B-D′) Representative immunofluorescence images of HRO at ages D100 to D160 showing spatial arrangement of DBCs and their neurite growth pattern (arrowhead, C). RBCs emerged as a subset of DBCs (arrow, D′). (E) Schematic showing characteristic features of HCs identified in HROs. (F-I′) Representative immunofluorescence images of HRO at ages D130 to D220 showing spatial arrangement of HCs (F-I′) and their neurite growth pattern (arrows, F-I). *n*, number of HROs evaluated at each age. Asterisk indicates nascent layers. Scale bars: 50 µm.

photoreceptors and morphogenesis of DBCs and HCs; the localization of presynaptic components to the OPL is a quantifiable representation of OPL state, characterized by progressive localization of bassoon to the OPL; and iPSC- and ESC-derived human retinal organoids replicate major features of early OPL maturation despite their heterogeneity and an apparent plateauing in their development. This study represents the first detailed analysis of early events in OPL morphogenesis and synaptogenesis in fetal retina and highlights the recapitulation of this process in HROs.

Development (2021) 148, dev199551. doi:10.1242/dev.199551

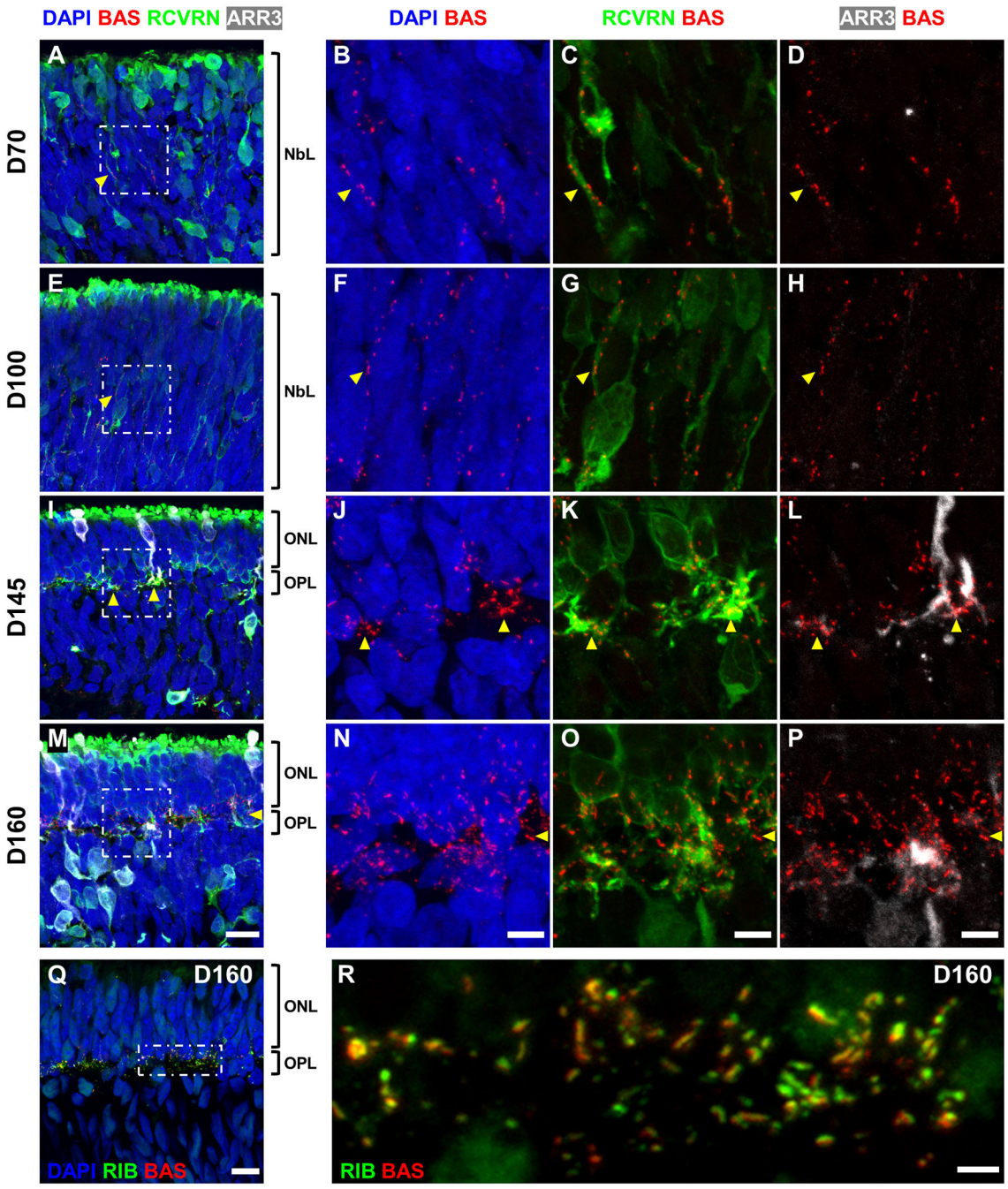

Fig. 9. Subcellular location of ribbon proteins in maturing photoreceptors during OPL formation in WTC11 iPSC-derived HROs. (A-P) Bassoon (BAS) transport to the OPL along RCRN$^+$ photoreceptors and ARR3$^+$ cones is observed from D70 to D160. Boxed regions in A, E, I and M are shown at higher magnification in B-D, F-H, J-L and N-P, respectively. Yellow arrowheads indicate subcellular trafficking of bassoon in maturing photoreceptors. (Q-R) Co-staining of bassoon and ribeye (RIB) at D160 shows colocalization of these proteins along the OPL (Q). Boxed region in Q is shown at higher magnification in R. Scale bars: 15 µm (A,E,I,M); 5 µm (B-D,F-H,J-L,N-P); 10 µm (Q); 2 µm (R).

The development of the first synapse of the visual system between photoreceptors, BCs and HCs at the OPL is a complex process requiring: laminar organization of retinal cells in the ONL and INL; bipolar and HC dendrite outgrowth and arborization within the OPL; trafficking of synaptic proteins to the OPL; assembly of ribbon synapses at photoreceptor terminals and apposition to postsynaptic proteins; and functional wiring of photoreceptors and BCs along rod and cone pathways (D'Orazi et al., 2014; Hoon et al., 2014; Pearring et al., 2013; Regus-Leidig et al., 2009; Schmitz, 2009; tom Dieck and Brandstätter, 2006). Many of these events have been studied in animal models, which laid the foundation for our understanding of development and disease pathogenesis in human retina (Hoon et al., 2014; Veleri et al., 2015). However, interspecies differences in retinal anatomy and functional specializations pose limitations for elucidating human-specific aspects of development and determining the relevance of pharmacological therapies in the disease state. To address these caveats in animal models, human fetal and adult retinal tissues have been used in histologic and 'omics' studies dissecting human eye development. Such studies have provided valuable insights into structural architecture (Hendrickson, 2016; Hendrickson and Drucker,

Development (2021) 148, dev199551. doi:10.1242/dev.199551

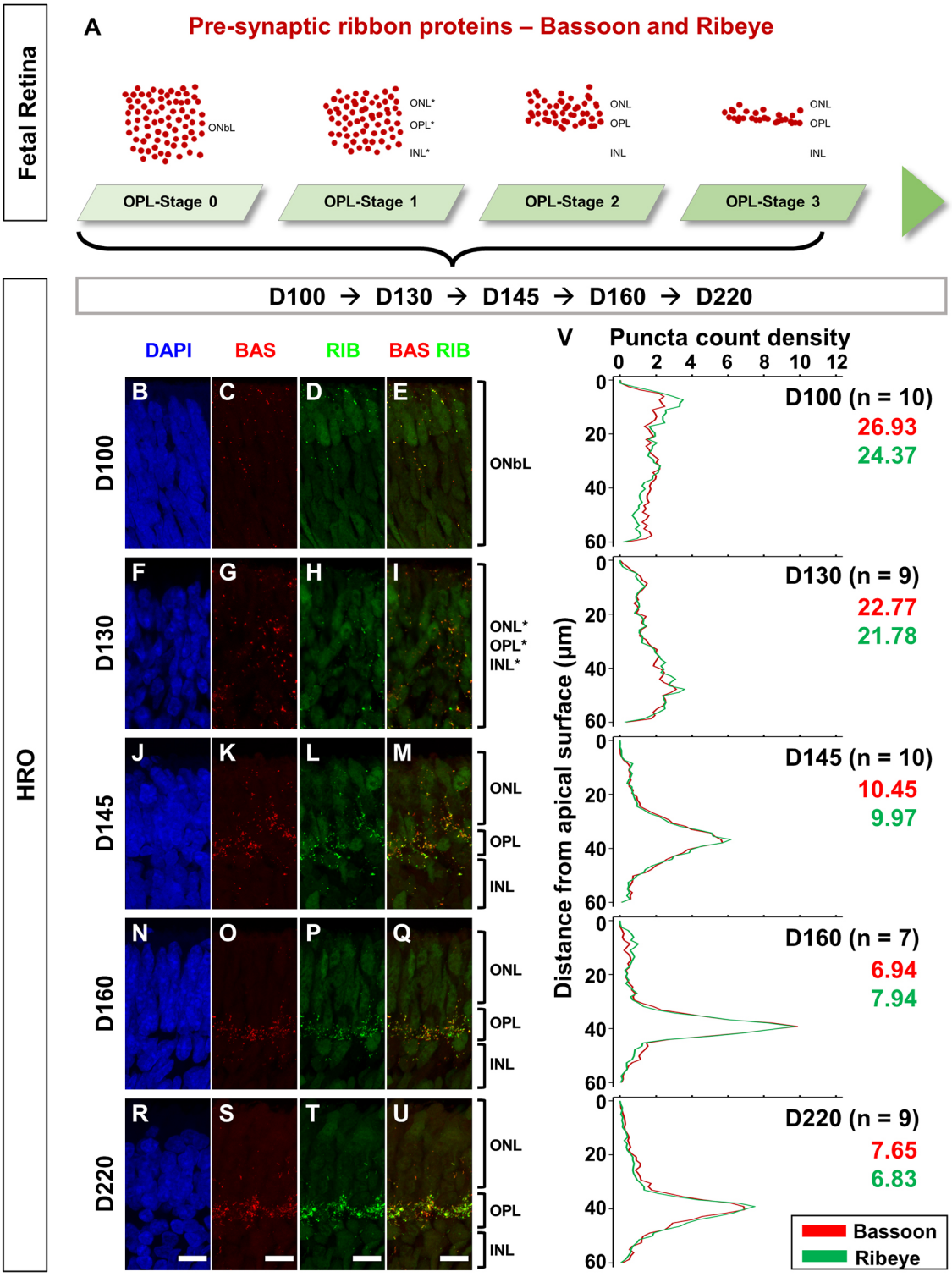

Fig. 10. Quantitative evaluation of bassoon and ribeye in WTC11 iPSC-derived HROs. (A) Schematic showing spatiotemporal expression pattern of bassoon and ribeye at OPL-Stages 0-3 in human fetal retina, which are recapitulated in HROs. (B-U) Representative maximum intensity projections of immunofluorescence images of HROs at ages D100 (B-E), D130 (F-I), D145 (J-M), D160 (N-Q) and D220 (R-U) showing progressive synaptic localization of bassoon and ribeye to the OPL. (V) Graphs showing bassoon (red) and ribeye (green) puncta count distributions along the apical-basal axis for each HRO age. Mean IQR values for bassoon and ribeye distributions are shown at the top right corner for each HRO age. *n*, number of regions analyzed at each age, taken from 5, 5, 6, 4 and 4 HROs at D100, D130, D145, D160 and D220, respectively, from 3-4 independent HRO preparations. Asterisk indicates nascent retinal layers. Scale bars: 10 µm.

1992; Hendrickson et al., 2012), temporal transcriptome dynamics (Cowan et al., 2020; Hoshino et al., 2017; Mellough et al., 2019; Ratnapriya et al., 2019; Sridhar et al., 2020) and chromatin accessibility dynamics (Xie et al., 2020) in healthy and diseased retina.

However, a tissue-based analysis of human OPL development has not been performed. We address this knowledge gap by identifying stages of photoreceptor, DBC and HC morphogenesis resulting in OPL formation (Figs 1 and 4). The DBC morphogenesis

Development (2021) 148, dev199551. doi:10.1242/dev.199551

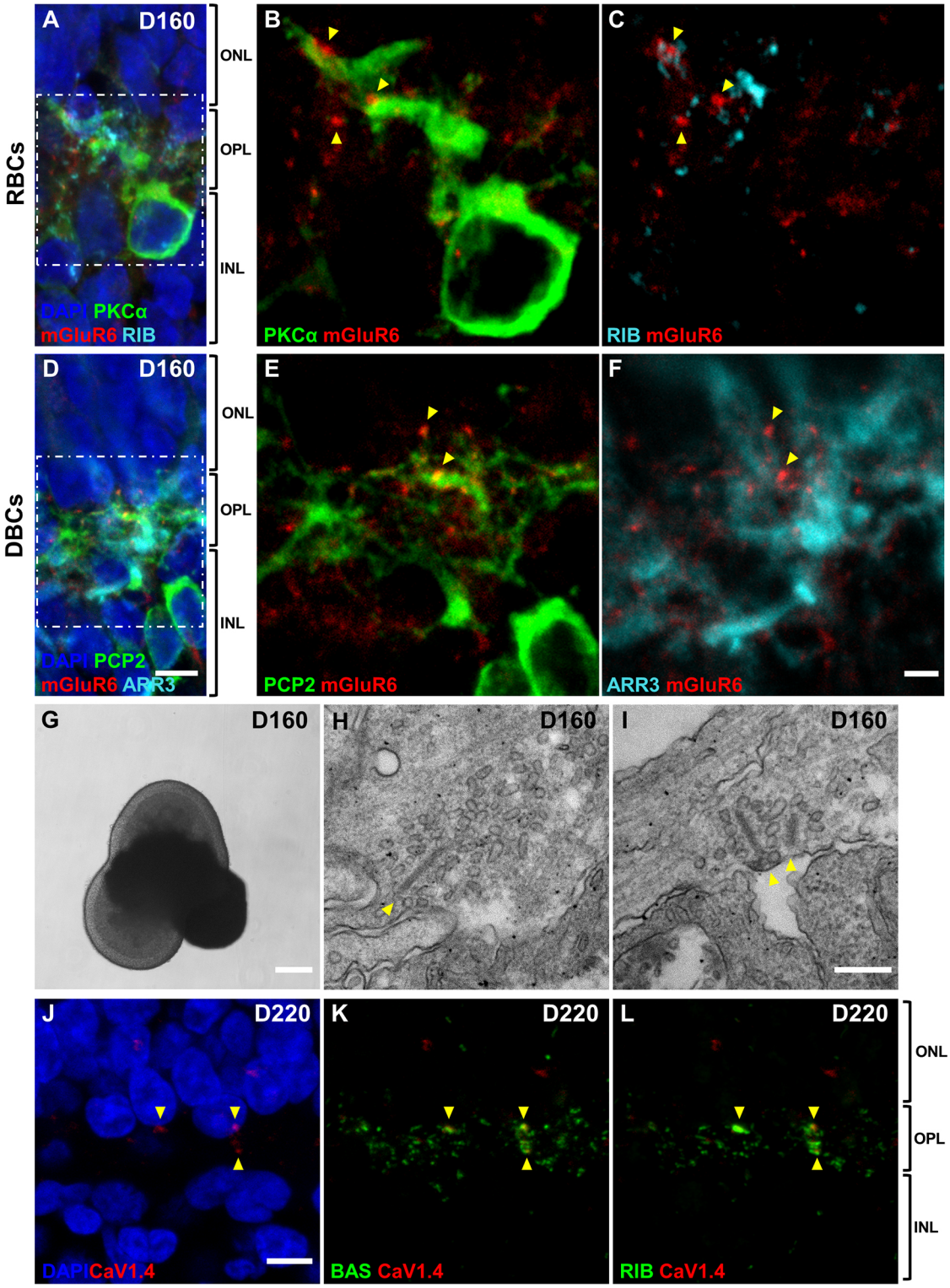

Fig. 11. Synaptic assembly in WTC11 iPSC-derived HROs. (A-F) Immunofluorescence images of D160 HRO showing mGluR6 expression at the OPL resembling OPL-Stage 3. Boxed regions in A and D are shown at higher magnification in B,C and E,F, respectively. mGluR6 puncta (arrowheads, B,C,E,F) on RBC (PKCα$^+$ in A,B) and DBC (PCP2$^+$ in D,E) dendrites are seen in proximity to ribeye (A,C) and cone terminals (ARR3$^+$ in D,F), respectively. (G) Light microscopy image of a live D160 HRO taken for transmission electron microscopy studies. (H,I) Transmission electron micrographs showing synaptic ribbons (arrowheads). (J-L) Expression of $Ca_v1.4$ at the OPL (arrowheads) and apposition to bassoon (K) and ribeye (L) at D220. Scale bars: 5 µm (A-F); 200 µm (G); 0.25 µm (H,I); 10 µm (J-L).

in human fetal retina along OPL stages 0 to 3 described here is similar to the dendrite growth pattern of this cell type in developing mouse retina from postnatal day (P)3 to P9 (Morgan et al., 2006). The OPL localization of bassoon and ribeye proteins in human fetal retina along five stages (Fig. 2) resembled precursor sphere-mediated transport of these ribbon proteins in developing mouse

Development (2021) 148, dev199551. doi:10.1242/dev.199551

retina (Regus-Leidig et al., 2009). Overall, the morphogenetic and synaptogenic events encompassed by OPL-Stage 0 to Stage 4 in human fetal retina parallel those of mouse retinal development from P0 to P8 (Morgan et al., 2006; Regus-Leidig et al., 2009). Therefore, the human OPL staging system described here may permit the investigation of the roles of specific cell types in initiating ribbon synapse assembly and establishing functional synapses. Furthermore, our analysis of bassoon and ribeye OPL localization (Fig. 3; Fig. S2) may provide a quantitative framework for assaying other aspects of retinal maturation, including cell subtype specification, neurite arborization and anterograde-retrograde cargo transport.

Given the limited availability of human fetal tissue, HRO production from pluripotent stem cells represents a viable *in vitro* model system to study normal development and disease pathogenesis. Systematic examination of developing HROs has established their potential to recapitulate crucial *in vivo* features of fetal retina tissue such as the temporal order of retinogenesis (Collin et al., 2019; Eldred et al., 2018; Sridhar et al., 2020) and laminar organization of cell types (Fig. 5; Kuwahara et al., 2015; Cowan et al., 2020; Zhong et al., 2014). Some of these studies extended their analysis to cell-specific features that can impart functionality such as outer segment formation (Cowan et al., 2020; Wahlin et al., 2017), phototransduction protein expression (Zhong et al., 2014), electrophysiological responses (Meyer et al., 2011; Zhong et al., 2014; Wahlin et al., 2017; Cowan et al., 2020) and ribbon synapse formation (Capowski et al., 2019; Cowan et al., 2020; Wahlin et al., 2017). HRO-based disease modeling thus far has been confined to the study of early-onset retinal dystrophies (Huang et al., 2019; Kruczek et al., 2021; Lukovic et al., 2020; Parfitt et al., 2016) that, for example, result in the dysfunction of the photoreceptor cilium necessary for outer segment formation. A recent study remarkably demonstrated that HRO photoreceptors form synaptic connections and encode visual stimuli along the OFF pathway (Cowan et al., 2020). There is a continued need to evaluate the potential of 'mini-retina' models to establish synaptic wiring and functional visual circuitry *in vitro*.

In a recent study, Capowski et al. (2019) addressed inter-organoid variability and the inadequacy of time in culture to directly reflect the maturation state of HROs. Our study reinforces the idea that time in culture must be coupled with morphological features to determine maturation stage (Figs 7, 8 and 10). Acknowledging these limitations, HRO regions were evaluated using our stage-based timeline of OPL development and the most mature feature of each cell type was chosen for analysis. We found that both ESC- and iPSC-derived HROs could recapitulate outer retinal lamination (Figs 5-8; Fig. S4), DBC and HC dendrite growth patterns (Fig. 8), and presynaptic protein localization (Figs 9,10; Fig. S7). In some D220 HROs, we could also detect the apposition of presynaptic proteins to mGluR6 and $Ca_v1.4$ (Fig. 11). This remarkable recapitulation of early synaptic development raises the possibility that these synapses may be functional and specific.

Though OPL-Stages 0 through 3 in HROs and fetal retinae showed striking similarity in their overall features, *in vitro* OPL assembly was not identical to fetal retina. The HROs had a narrower OPL at all stages, variable rod-to-cone ratios, non-uniform distribution of HCs and DBCs, and no identifiable IPL. We also observed that cellular maturation in the ONL and INL within HROs was not as synchronized as in fetal retina. Many factors are likely to contribute to these disparities. HRO production relies predominantly on self-assembly in the absence of developmental gradients, surrounding tissues and mechanosensory cues. Furthermore, RGC numbers dwindle as BCs are maturing (Fig. S6D,F,H,J,L,N; Aparicio et al., 2017; Capowski et al., 2019). The need for improved protocols that promote synaptic maturation and long-term maintenance is well acknowledged in the field. Advances in retinal pigment epithelium (RPE)-organoid co-culture, organoid-on-a-chip and extracellular matrix formulations hold great promise (Achberger et al., 2019).

In conclusion, the OPL staging system reported in this study provides a practical and quantifiable means to identify and compare similarly developed retinal regions, and thus to evaluate the effect of genetic or pharmacological manipulations in the organoid system. By complementing an existing global HRO staging system with OPL-specific features, our staging system facilitates a more detailed dissection of outer retinal morphogenesis and synaptogenesis. Future studies have the potential to go beyond structural characterization in fixed organoids and use live imaging strategies or tests for synaptic function using patch-clamp or imaging-based electrophysiology methods.

MATERIALS AND METHODS

Pluripotent stem cell culture and retinal organoid differentiation

The WTC11 iPSC line (GM25256, Coriell Institute) and H9 (WAe009, Wicell) were maintained in standard feeder-free culture conditions on human ESC qualified Matrigel (Stem Cell Technologies)-coated tissue culture dishes in mTeSR1 media (Stem Cell Technologies). For HRO generation, a previously described protocol (Zhong et al., 2014) with the following minor modifications was carried out. Briefly, on day of retinal culture initiation (D0), iPSCs and ESCs were pretreated with 10 µM blebbistatin (Sigma-Aldrich) in mTeSR1 medium for 1 h, and then enzymatically detached by Accutase (Stem Cell Technologies) treatment for 8-12 min. On D70, 1 µM all-trans retinoic acid (Sigma-Aldrich) was added to the long-term suspension culture medium to promote photoreceptor maturation, then decreased to 0.5 µM indefinitely from D98. At each sampling age, four to six organoids with the desired light microscopic appearance [Stage 2 at D100 and maturing to Stage 3 through D130, D145, D160, D220 and D280 per Capowski et al. (2019)] were selected from eight to ten HRO preparations using a Nikon SM21500 stereomicroscope.

Human fetal retina sections

All human fetal samples were collected under Institutional Review Board approval (USC-HS-13-0399, CHLA-14-2211 and CHLA-15-00363). Following the patient decision for pregnancy termination, the patient was offered the option of donation of the products of conception for research purposes, and those that agreed signed an informed consent. This did not alter the choice of termination procedure, and the products of conception from those that declined participation were disposed of in a standard fashion. The only information collected was gestational age and whether there were any known genetic or structural abnormalities. All tissues were studied in compliance with the tenets of the Declaration of Helsinki. Fetal age was determined based on American College of Obstetrics and Gynecology guidelines (Pettker et al., 2017). The cornea and lens were removed and the eyes fixed in 4% paraformaldehyde in 1× PBS at room temperature (RT) for 30 min, incubated in 30% sucrose in 1× PBS at 4°C for 15 min, embedded in two parts 30% sucrose in 1× PBS and one part optimal cutting temperature compound (OCT; Miles Laboratories), frozen, and sectioned at 10 µm. The slides were stored at −80°C.

Immunofluorescence staining

A previously described protocol was used for fixation of HROs and preparation of frozen tissue sections (Aparicio et al., 2017). HRO immunostaining was performed on 20 µm thick OCT sections on glass slides using a published protocol (Wakeham et al., 2020) with modifications. The frozen sections were thawed at RT and then permeabilized and blocked for 1 h in a humidified chamber at RT with 1× PBS containing 3% horse serum and 0.3% Triton X-100. This was followed by incubation with primary antibodies diluted in blocking buffer for 2 h at RT. After rinsing with 1× PBS thrice, the slides were incubated with

Development (2021) 148, dev199551. doi:10.1242/dev.199551

AlexaFluor-conjugated secondary antibodies in blocking buffer for 1 h at RT. To visualize cell nuclei, 5 µg/ml DAPI (Invitrogen) was added to 1× PBS in the final wash step. The immunostained tissue sections were mounted with a coverslip in Prolong Mountant Media (Thermo Fisher Scientific) and sealed. Primary and secondary antibodies are listed in Table S1.

Confocal fluorescence microscopy

Confocal *z*-stacks were acquired with an LSM 700 system (Carl Zeiss Microscopy) mounted on an Axio Observer.Z1 microscope equipped with Plan-APOCHROMAT 10×/0.45, 20×/0.8 and 63×/1.4 (oil-immersion) lenses. Laser light of 405, 488, 555 and 639 nm was used to excite fluorescence of DAPI and Alexa Fluor 488, 568 and 647, respectively. The pinhole size was 1 Airy unit for each channel and the voxel sizes were 0.39×0.39×3.13 µm^3 for all 10×, 0.20×0.20×0.87 µm^3 for all 20× and 0.06×0.06×0.34 µm^3 for all 63× images, except 63× images of fetal retina which had voxels of 0.08×0.08×0.34 µm^3. The laser power and gain were adjusted to maximize dynamic range without saturating any pixels. After image capture, brightness adjustments, image cropping, channel overlays and maximum intensity projections were generated using FIJI ImageJ software (Schindelin et al., 2012). For OPL staging, 250 µm×200 µm ROI on maximum intensity projections of four to nine optical sections at 20× were analyzed (Figs 1,7,8,10; Figs S1,S2). For qualitative study of synaptic protein localization in fetal retina, 100 µm×100 µm ROI on maximum intensity projections 12 optical sections at 63× were analyzed (Figs 2 and 3). The cellular features of retinal cell types relative to each other were identified by observing corresponding regions on serial sections. The same imaging parameters and signal enhancements were used for each marker across all stages or ages.

Transmission electron microscopy

Samples were fixed at room temperature with 2.5% glutaraldehyde, 2% paraformaldehyde and 7% sucrose in 0.1 M HEPES buffer (pH 7.3). After 1 h in fix, the samples were stored in the fixative at 4°C. Post fixation, the samples were rinsed three times in 0.1 M HEPES before incubating in 2% osmium tetroxide for a minimum of 2 h. Before *en bloc* staining with 1% uranyl acetate (aq), samples were rinsed thrice for 15 min with ultra-pure water. After an overnight incubation at 4°C, the samples were rinsed twice in ultra-pure water, then gradually dehydrated in a graded ethanol series (50%, 70%, 90%, 100%, 100%, 100%), all eight steps at 10 min each. Two quick rinses in propylene oxide were used as a transition to infiltration with Eponate 12 (Ted Pella) starting with 1:1 propylene oxide to epoxy for 1 h, 2:1 for 1 h, and then pure epoxy overnight. The next day two 1 h incubations in fresh epoxy were made before the samples were arranged in molds and polymerized at 60°C for 18 h. Polymerized blocks were trimmed by hand with a razor blade then sectioned on a Leica LC6 ultramicrotome initially at 1 micron to find the area of interest. Then thin sections (70 nm) were picked up on formvar and carbon coated copper grids. Grids were stained with lead citrate followed by uranyl acetate. Images were taken on a FEI (Thermo Fisher Scientific) Talos F200C at 80KeV with a Ceta 4K CMOS camera.

Acknowledgements

We acknowledge the Children's Hospital Los Angeles Stem Cell Analytics Core and Cellular Imaging Core for providing key instrumentation and personnel to support this work. Electron microscopy was performed at the Core Center of Excellence in Nano Imaging at the University of Southern California. We thank Andrew Salas for maintenance of human iPSC and ESC lines. We thank Hardeep P. Singh and Dominic Shayler for providing human fetal retina sections and for reviewing the manuscript. We appreciate helpful feedback on the manuscript from Pat Levitt and members of his laboratory. We thank Melissa L. Wilson (Department of Preventive Medicine, University of Southern California) and Family Planning Associates for coordinating fetal tissue collection. We thank Catherine W. Morgans (Oregon Health & Science University) for advice on immunofluorescence methods and for generously providing $Ca_V1.4$ antibody.

Competing interests

The authors declare no competing or financial interests.

Author contributions

Conceptualization: S.P.B., A.N.; Methodology: S.P.B., A.F., K.S., G.E.F., M.W.R., N.H., C.M., M.E.T., J.G.A.; Software: G.E.F., M.W.R.; Validation: S.P.B., A.N.; Formal analysis: S.P.B., G.E.F., M.W.R., J.S.K., C.H., C.M., A.N.; Investigation: S.P.B., A.N.; Resources: C.M., B.H.G., D.C., J.G.A., A.N.; Data curation: S.P.B., G.E.F., M.W.R., J.S.K., C.H.; Writing - original draft: S.P.B., A.N.; Writing - review & editing: S.P.B., D.C., J.G.A., A.N.; Visualization: S.P.B., A.N.; Supervision: A.N.; Project administration: A.N.; Funding acquisition: D.C., A.N.

Funding

This research was supported in part by: an unrestricted grant to the Department of Ophthalmology at the Keck School of Medicine of USC from Research to Prevent Blindness, New York, NY, USA (A.N.), a National Eye Institute Career Development Award K08EY030924 (A.N.), the Las Madrinas Endowment in Experimental Therapeutics for Ophthalmology (A.N.), the Knights Templar Eye Foundation (A.N.), the Donald E. and Delia B. Baxter Foundation (A.N.), a Research to Prevent Blindness Career Development Award (A.N.), a Saban Research Institute of Children's Hospital Los Angeles Core Facility Pilot grant (A.N.), The Leon and Carol Ellison Research Career Development Award at The Saban Research Institute of Children's Hospital Los Angeles (A.N.), the Neonatal Blindness Research Fund at Children's Hospital Los Angeles (J.G.A., D.C.), and National Institutes of Health grant R01EY026661 (D.C.). J.S.K. was supported by the Sigma Xi Research Aid Grant and Dean's Undergraduate Research Fund, New York University, NY, USA. Deposited in PMC for release after 12 months.

Peer review history

The peer review history is available online at https://journals.biologists.com/dev/article-lookup/doi/10.1242/dev.199551

References

Achberger, K., Probst, C., Haderspeck, J., Bolz, S., Rogal, J., Chuchuy, J., Nikolova, M., Cora, V., Antkowiak, L., Haq, W. et al. (2019). Merging organoid and organ-on-a-chip technology to generate complex multi-layer tissue models in a human retina-on-a-chip platform. *eLife* **8**:e46188. doi:10.7554/eLife.46188

Aparicio, J. G., Hopp, H., Choi, A., Mandayam Comar, J., Liao, V. C., Harutyunyan, N. and Lee, T. C. (2017). Temporal expression of CD184(CXCR4) and CD171(L1CAM) identifies distinct early developmental stages of human retinal ganglion cells in embryonic stem cell derived retina. *Exp. Eye Res.* **154**, 177-189. doi:10.1016/j.exer.2016.11.013

Browne, A. W., Arnesano, C., Harutyunyan, N., Khuu, T., Carlos, J., Pollack, H. A., Koos, D. S., Lee, T. C., Fraser, S. E., Aparicio, J. G. et al. (2017). Structural and functional characterization of human stem-cell-derived retinal organoids by live imaging. *Invest. Ophthalmol. Vis. Sci.* **58**, 3311-3318.

Cao, Y., Sarria, I., Fehlhaber, K. E., Kamasawa, N., Orlandi, C., James, K. N., Hazen, J. L., Gardner, M. R., Farzan, M., Lee, A. et al. (2015). Mechanism for selective synaptic wiring of rod photoreceptors into the retinal circuitry and its role in vision. *Neuron* **87**, 1248-1260. doi:10.1016/j.neuron.2015.09.002

Capowski, E. E., Samimi, K., Mayerl, S. J., Phillips, M. J., Pinilla, I., Howden, S. E., Saha, J., Jansen, A. D., Edwards, K. L., Jager, L. D. et al. (2019). Reproducibility and staging of 3D human retinal organoids across multiple pluripotent stem cell lines. *Development* **146**, dev171686. doi:10.1242/dev.171686

Clark, B. S., Stein-O'Brien, G. L., Shiau, F., Cannon, G. H., Davis-Marcisak, E., Sherman, T., Santiago, C. P., Hoang, T. V., Rajaii, F., James-Esposito, R. E. et al. (2019). Single-Cell RNA-seq analysis of retinal development identifies NFI factors as regulating mitotic exit and late-born cell specification. *Neuron* **102**, 1111-1126.e5. doi:10.1016/j.neuron.2019.04.010

Collin, J., Queen, R., Zerti, D., Dorgau, B., Hussain, R., Coxhead, J., Cockell, S. and Lako, M. (2019). Deconstructing retinal organoids: single cell RNA-seq reveals the cellular components of human pluripotent stem cell-derived retina: deconstructing retinal organoids. *Stem Cells* **37**, 593-598. doi:10.1002/stem.2963

Cowan, C. S., Renner, M., De Gennaro, M., Gross-Scherf, B., Goldblum, D., Hou, Y., Munz, M., Rodrigues, T. M., Krol, J., Szikra, T. et al. (2020). Cell types of the human retina and its organoids at single-cell resolution. *Cell* **182**, 1623-1640.e34. doi:10.1016/j.cell.2020.08.013

D'Orazi, F. D., Suzuki, S. C. and Wong, R. O. (2014). Neuronal remodeling in retinal circuit assembly, disassembly, and reassembly. *Trends Neurosci.* **37**, 594-603. doi:10.1016/j.tins.2014.07.009

Dowling, J. E. (2009). Retina: an overview. In *Encyclopedia of Neuroscience* (ed. L. R. Squire), pp. 159-169. Academic Press.

Eldred, K. C., Hadyniak, S. E., Hussey, K. A., Brenerman, B., Zhang, P.-W., Chamling, X., Sluch, V. M., Welsbie, D. S., Hattar, S., Taylor, J. et al. (2018). Thyroid hormone signaling specifies cone subtypes in human retinal organoids. *Science* **362**, eaau6348. doi:10.1126/science.aau6348

Gasparini, S. J., Llonch, S., Borsch, O. and Ader, M. (2019). Transplantation of photoreceptors into the degenerative retina: current state and future perspectives. *Prog. Retin. Eye Res.* **69**, 1-37. doi:10.1016/j.preteyeres.2018.11.001

Hallam, D., Hilgen, G., Dorgau, B., Zhu, L., Yu, M., Bojic, S., Hewitt, P., Schmitt, M., Uteng, M., Kustermann, S. et al. (2018). Human-induced pluripotent stem cells generate light responsive retinal organoids with variable and nutrient-dependent efficiency: generating light responsive retinal organoids from iPSC. *Stem Cells* **36**, 1535-1551. doi:10.1002/stem.2883

Haverkamp, S. (2006). Synaptic plasticity in CNGA3-/- mice: cone bipolar cells react on the missing cone input and form ectopic synapses with rods. *J. Neurosci.* **26**, 5248-5255. doi:10.1523/JNEUROSCI.4483-05.2006

Hendrickson, A. (2016). Development of retinal layers in prenatal human retina. *Am. J. Ophthalmol.* **161**, 29-35.e1. doi:10.1016/j.ajo.2015.09.023

Hendrickson, A. and Drucker, D. (1992). The development of parafoveal and mid-peripheral human retina. *Behav. Brain Res.* **49**, 21-31. doi:10.1016/S0166-4328(05)80191-3

Hendrickson, A. and Zhang, C. (2019). Development of cone photoreceptors and their synapses in the human and monkey fovea. *J. Comp. Neurol.* **527**, 38-51. doi:10.1002/cne.24170

Hendrickson, A., Possin, D., Vajzovic, L. and Toth, C. A. (2012). Histologic development of the human fovea from midgestation to maturity. *Am. J. Ophthalmol.* **154**, 767-778.e2. doi:10.1016/j.ajo.2012.05.007

Hoon, M., Okawa, H., Della Santina, L. and Wong, R. O. L. (2014). Functional architecture of the retina: Development and disease. *Prog. Retin. Eye Res.* **42**, 44-84. doi:10.1016/j.preteyeres.2014.06.003

Hoshino, A., Ratnapriya, R., Brooks, M. J., Chaitankar, V., Wilken, M. S., Zhang, C., Starostik, M. R., Gieser, L., La Torre, A., Nishio, M. et al. (2017). Molecular anatomy of the developing human retina. *Dev. Cell* **43**, 763-779.e4. doi:10.1016/j.devcel.2017.10.029

Huang, K.-C., Wang, M.-L., Chen, S.-J., Kuo, J.-C., Wang, W.-J., Nhi Nguyen, P. N., Wahlin, K. J., Lu, J.-F., Tran, A. A., Shi, M. et al. (2019). Morphological and molecular defects in human three-dimensional retinal organoid model of X-linked juvenile retinoschisis. *Stem Cell Rep.* **13**, 906-923. doi:10.1016/j.stemcr.2019.09.010

Jones, B. W. and Marc, R. E. (2005). Retinal remodeling during retinal degeneration. *Exp. Eye Res.* **81**, 123-137. doi:10.1016/j.exer.2005.03.006

Jones, B. W., Kondo, M., Terasaki, H., Lin, Y., McCall, M. and Marc, R. E. (2012). Retinal remodeling. *Jpn. J. Ophthalmol.* **56**, 289-306. doi:10.1007/s10384-012-0147-2

Kruczek, K., Qu, Z., Gentry, J., Fadl, B. R., Gieser, L., Hiriyanna, S., Batz, Z., Samant, M., Samanta, A., Chu, C. J. et al. (2021). Gene therapy of dominant CRX-Leber congenital amaurosis using patient stem cell-derived retinal organoids. *Stem Cell Rep.* **16**, 252-263. doi:10.1016/j.stemcr.2020.12.018

Kuwahara, A., Ozone, C., Nakano, T., Saito, K., Eiraku, M. and Sasai, Y. (2015). Generation of a ciliary margin-like stem cell niche from self-organizing human retinal tissue. *Nat. Commun.* **6**, 6286-6301. doi:10.1038/ncomms7286

Lukovic, D., Artero Castro, A., Kaya, K. D., Munezero, D., Gieser, L., Davó-Martínez, C., Corton, M., Cuenca, N., Swaroop, A., Ramamurthy, V. et al. (2020). Retinal Organoids derived from hiPSCs of an AIPL1-LCA Patient Maintain Cytoarchitecture despite Reduced levels of Mutant AIPL1. *Sci. Rep.* **10**, 5426. doi:10.1038/s41598-020-62047-2

Mellough, C. B., Bauer, R., Collin, J., Dorgau, B., Zerti, D., Dolan, D. W. P., Jones, C. M., Izuogu, O. G., Yu, M., Hallam, D. et al. (2019). An integrated transcriptional analysis of the developing human retina. *Development* **146**, dev169474. doi:10.1242/dev.169474

Meyer, J. S., Howden, S. E., Wallace, K. A., Verhoeven, A. D., Wright, L. S., Capowski, E. E., Pinilla, I., Martin, J. M., Tian, S., Stewart, R. et al. (2011). Optic vesicle-like structures derived from human pluripotent stem cells facilitate a customized approach to retinal disease treatment. *Stem Cells* **29**, 1206-1218. doi:10.1002/stem.674

Morgan, J. L., Dhingra, A., Vardi, N. and Wong, R. O. L. (2006). Axons and dendrites originate from neuroepithelial-like processes of retinal bipolar cells. *Nat. Neurosci.* **9**, 85-92. doi:10.1038/nn1615

Mumm, J. S., Godinho, L., Morgan, J. L., Oakley, D. M., Schroeter, E. H. and Wong, R. O. L. (2005). Laminar circuit formation in the vertebrate retina. *Prog. Brain Res.* **147**, 155-169. doi:10.1016/S0079-6123(04)47012-5.

Nakano, T., Ando, S., Takata, N., Kawada, M., Muguruma, K., Sekiguchi, K., Saito, K., Yonemura, S., Eiraku, M. and Sasai, Y. (2012). Self-formation of optic cups and storable stratified neural retina from human ESCs. *Cell Stem Cell* **10**, 771-785. doi:10.1016/j.stem.2012.05.009

O'Hara-Wright, M. and Gonzalez-Cordero, A. (2020). Retinal organoids: a window into human retinal development. *Development* **147**, dev189746. doi:10.1242/dev.189746

Parfitt, D. A., Lane, A., Ramsden, C. M., Carr, A.-J. F., Munro, P. M., Jovanovic, K., Schwarz, N., Kanuga, N., Muthiah, M. N., Hull, S. et al. (2016). Identification and correction of mechanisms underlying inherited blindness in human iPSC-derived optic cups. *Cell Stem Cell* **18**, 769-781. doi:10.1016/j.stem.2016.03.021

Pearring, J. N., Salinas, R. Y., Baker, S. A. and Arshavsky, V. Y. (2013). Protein sorting, targeting and trafficking in photoreceptor cells. *Prog. Retin. Eye Res.* **36**, 24-51. doi:10.1016/j.preteyeres.2013.03.002

Peng, Y.-W., Hao, Y., Petters, R. M. and Wong, F. (2000). Ectopic synaptogenesis in the mammalian retina caused by rod photoreceptor-specific mutations. *Nat. Neurosci.* **3**, 1121-1127. doi:10.1038/80639

Pettker, C., Goldberg, J., El-Sayed, Y. and Copel, J. (2017). Committee opinion no 700: Methods for estimating the due date. *Obstet. Gynecol.* **129**, e150-e154. doi:10.1097/AOG.0000000000002046

Phillips, M. J., Capowski, E. E., Petersen, A., Jansen, A. D., Barlow, K., Edwards, K. L. and Gamm, D. M. (2018). Generation of a rod-specific NRL reporter line in human pluripotent stem cells. *Sci. Rep.* **8**, 2370. doi:10.1038/s41598-018-20813-3

Ratnapriya, R., Sosina, O. A., Starostik, M. R., Kwicklis, M., Kapphahn, R. J., Fritsche, L. G., Walton, A., Arvanitis, M., Gieser, L., Pietraszkiewicz, A. et al. (2019). Retinal transcriptome and eQTL analyses identify genes associated with age-related macular degeneration. *Nat. Genet.* **51**, 606-610. doi:10.1038/s41588-019-0351-9

Rattner, A., Sun, H. and Nathans, J. (1999). Molecular genetics of human retinal disease. *Annu. Rev. Genet.* **33**, 89-131. doi:10.1146/annurev.genet.33.1.89

Regus-Leidig, H., tom Dieck, S., Specht, D., Meyer, L. and Brandstätter, J. H. (2009). Early steps in the assembly of photoreceptor ribbon synapses in the mouse retina: The involvement of precursor spheres. *J. Comp. Neurol.* **512**, 814-824. doi:10.1002/cne.21915

Sarria, I., Cao, Y., Wang, Y., Ingram, N. T., Orlandi, C., Kamasawa, N., Kolesnikov, A. V., Pahlberg, J., Kefalov, V. J., Sampath, A. P. et al. (2018). LRIT1 modulates adaptive changes in synaptic communication of cone photoreceptors. *Cell Rep.* **22**, 3562-3573. doi:10.1016/j.celrep.2018.03.008

Schindelin, J., Arganda-Carreras, I., Frise, E., Kaynig, V., Longair, M., Pietzsch, T., Preibisch, S., Rueden, C., Saalfeld, S., Schmid, B. et al. (2012). Fiji: an open-source platform for biological-image analysis. *Nat. Methods* **9**, 676-682. doi:10.1038/nmeth.2019

Schmitz, F. (2009). The making of synaptic ribbons: how they are built and what they do. *Neuroscientist* **15**, 611-624. doi:10.1177/1073858409340253

Singh, M. S., Park, S. S., Albini, T. A., Canto-Soler, M. V., Klassen, H., MacLaren, R. E., Takahashi, M., Nagiel, A., Schwartz, S. D. and Bharti, K. (2020). Retinal stem cell transplantation: balancing safety and potential. *Prog. Retin. Eye Res.* **75**, 100779. doi:10.1016/j.preteyeres.2019.100779

Soto, F. and Kerschensteiner, D. (2015). Synaptic remodeling of neuronal circuits in early retinal degeneration. *Front. Cell. Neurosci.* **9**, 395. doi:10.3389/fncel.2015.00395

Sridhar, A., Hoshino, A., Finkbeiner, C. R., Chitsazan, A., Dai, L., Haugan, A. K., Eschenbacher, K. M., Jackson, D. L., Trapnell, C., Bermingham-McDonogh, O. et al. (2020). Single-cell transcriptomic comparison of human fetal retina, hPSC-derived retinal organoids, and long-term retinal cultures. *Cell Rep.* **30**, 1644-1659.e4. doi:10.1016/j.celrep.2020.01.007

tom Dieck, S. and Brandstätter, J. H. (2006). Ribbon synapses of the retina. *Cell Tissue Res.* **326**, 339-346. doi:10.1007/s00441-006-0234-0

Veleri, S., Lazar, C. H., Chang, B., Sieving, P. A., Banin, E. and Swaroop, A. (2015). Biology and therapy of inherited retinal degenerative disease: insights from mouse models. *Dis. Model. Mech.* **8**, 109-129. doi:10.1242/dmm.017913

Wahlin, K. J., Maruotti, J. A., Sripathi, S. R., Ball, J., Angueyra, J. M., Kim, C., Grebe, R., Li, W., Jones, B. W. and Zack, D. J. (2017). Photoreceptor outer segment-like structures in long-term 3D retinas from human pluripotent stem cells. *Sci. Rep.* **7**, 766-781. doi:10.1038/s41598-017-00774-9

Wakeham, C. M., Ren, G. and Morgans, C. W. (2020). Expression and distribution of trophoblast glycoprotein in the mouse retina. *J. Comp. Neurol.* **528**, 1660-1671. doi:10.1002/cne.24850

Wang, Y., Fehlhaber, K. E., Sarria, I., Cao, Y., Ingram, N. T., Guerrero-Given, D., Throesch, B., Baldwin, K., Kamasawa, N., Ohtsuka, T. et al. (2017). The auxiliary calcium channel subunit $\alpha 2\delta 4$ is required for axonal elaboration, synaptic transmission, and wiring of rod photoreceptors. *Neuron* **93**, 1359-1374.e6. doi:10.1016/j.neuron.2017.02.021

Wu, S. M. (2010). Synaptic organization of the vertebrate retina: general principles and species-specific variations: the friedenwald lecture. *Investig. Opthalmology Vis. Sci.* **51**, 1264. doi:10.1167/iovs.09-4396

Xie, H., Zhang, W., Zhang, M., Akhtar, T., Li, Y., Yi, W., Sun, X., Zuo, Z., Wei, M., Fang, X. et al. (2020). Chromatin accessibility analysis reveals regulatory dynamics of developing human retina and hiPSC-derived retinal organoids. *Sci. Adv.* **6**, eaay5247. doi:10.1126/sciadv.aay5247

Zhong, X., Gutierrez, C., Xue, T., Hampton, C., Vergara, M. N., Cao, L.-H., Peters, A., Park, T. S., Zambidis, E. T., Meyer, J. S. et al. (2014). Generation of three-dimensional retinal tissue with functional photoreceptors from human iPSCs. *Nat. Commun.* **5**, 4047. doi:10.1038/ncomms5047

Supplementary Materials and Methods

Bassoon and Ribeye quantification

For Bassoon and Ribeye quantification, 12 consecutive optical sections from each 63× z-stack were selected. The images were oriented with the photoreceptors on top and coordinate origin (0,0,0) set to the top left corner of the first z-slice. Fluorescent puncta were quantified along the Y direction by two methods using FIJI ImageJ software (Schindelin et al., 2012): (1) summing intensities of Bassoon for fetal retinae and WTC11 iPSC-derived HROs in a 30 µm × 60 µm × 2.01 µm ROIs and (2) manual counting of Bassoon and Ribeye puncta for WTC11 iPSC-derived HROs in a 30 µm × 60 µm × 4.03 µm ROIs in each XZ plane.

For the automated summed-intensity method, the Alexa Fluor 568 channels were background-subtracted with a rolling ball radius of 3 pixels, a Find Maxima filter with an appropriate prominence between 10 to 20 was applied, the resulting single-point ROIs were dilated 3×, and background-subtracted intensity within the dilated ROIs was summed in each XZ plane. Intensity summing was restricted to 60 µm along the apical-basal axis to avoid capturing Bassoon signals from the IPL. Intensity-based quantification of Ribeye could not be reliably performed due to overwhelming nuclear signal detected by the Ribeye/CtBP2 antibody, which also labels the nuclear isoform of the protein. Manual counting could not be performed on fetal retina due to coalescence of spots that hindered them from being distinguished. During manual counting of Bassoon and Ribeye puncta in WTC11 iPSC-derived HROs, puncta were tracked in adjacent sections to ensure each punctum was counted only once. The fluorescent spots with intensity values 10 and above were counted as puncta. Manual counting was performed by two trained masked graders (JSK and CH).

Statistical analysis of Bassoon and Ribeye OPL targeting

After identification of 3-dimensional coordinates of all Bassoon or Ribeye puncta, coordinate values were standardized and examined relative to each axis. The puncta count and puncta intensity data from the X- and Z-axes were randomly distributed and otherwise unremarkable.

To visualize and evaluate spatial distribution of puncta in each stage, density plots were generated using Epanechnikov kernel function with bandwidths of 1 for intensity data (Fig. S3A, Fig. S8B) and 0.5 for count data (Fig. 10V). To create puncta intensity density plots (Fig. S3A,

Fig. S8B), average intensity for each pixel was rounded to the nearest whole number, converted to an intensity "pseudo-count" per pixel per stage or age and then, these "pseudo-counts" were averaged and rounded to the nearest whole number. To create puncta count density plots (Fig. 10V), the count values at each pixel for images belonging to a specific age were averaged and rounded to the nearest whole number. Density values on plots report the relative percentage of puncta intensity (Fig. S3A and Fig. S8B) or puncta count (Fig. 10V) present at any position along the Y-axis.

Interquartile range (IQR) for puncta density distributions was calculated for each image (ROIs corresponding to data shown in Fig. S3A, Fig. 10V, Fig. S8B). IQR describes the dispersion of sample data and it is measured as (Q3-Q1), where Q3 and Q1 are data values at 75^{th} percentile and 25^{th} percentile of the distribution respectively. IQR values of puncta density distributions for each image are displayed in boxplots (Fig. 2U and Fig. S8A), with individual IQR values plotted by OPL stages (0 to 4, Fig. 2U) or HRO ages (D100 to D220, Fig. S8A). Boxplots shows median values (middle bars), and first to third interquartile ranges (boxes); whiskers indicate adjacent values located within 1.5 times the interquartile range; dots represent individual images. In this study, IQR expressed in μm represents the extent of puncta dispersion along the apical-basal axis. Higher IQR indicates puncta dispersion and lower IQR indicates puncta aggregation. Based on preliminary imaging data of Bassoon puncta, a power calculation was performed to determine the number of samples needed to observe a significant difference in IQR between HRO Day 130 and Day 160 (IQR Difference=15 μm, Effect Size=2.4). Assuming a Type I error rate of 5% and a Type II error rate of 20% (i.e., 80% Power), IQR values from at least 5 images per HRO age group are required to observe a significant effect of this magnitude.

To compare puncta intensity or count distribution between fetal retina stages (data shown in Fig. S3A), between HRO ages (data shown in Fig. 10V) or between HRO age and fetal retina stages (data shown in Fig. S8B and Fig. S3A), IQR values from each image were examined using restricted maximum likelihood linear mixed models (REML-LMM) with pairwise post-hoc comparisons (Fig. S3B, Fig. S8C). REML-LMM allow for examination of fixed effects while accounting for random variation present in each image. Significant *p* values from omnibus *F*-tests of these models were used to describe global changes in puncta data over ages/stages. Significant *p* values from pairwise comparisons denoted unique IQR values, and, therefore, significant changes in puncta organization between individual stages/ages. Images were excluded

from analysis if the calculated IQR values were more than 2 standard deviations from the mean IQR value of the image set with the excluded image removed. Using this criteria, one image from Day 130, two images from Day 160, and one image from Day 220 were removed from analysis of puncta count and intensity data.

Because of the large number of comparisons conducted on puncta data, the Holm-Bonferroni correction (Holm, 1979) was used on 84 tests of these data with a family-wise Type I error rate of 0.05, resulting in all tests with p values <0.001 being considered statistically significant. All analyses were conducted using Stata/SE 14.2 (StataCorp LLC, College Station, Texas).

Quantification of inter- and intra-organoid variability

In order to measure variability observed on HRO sections, cellular features of the two major retinal cell types associated with OPL formation that were found in variable counts and maturation states—horizontal cells ($CALB^+$), and DBCs ($PCP2^+$)—were selected for quantification. Within each randomly selected ROI, the maturation state of each cell type was scored on a three-point scale, where 0 indicates an absence or nascent state (equivalent to up to OPL-Stage 0), 1 indicates mid-maturation state (OPL-stage 1 or OPL-Stage 2), and 2 indicates a mature state (OPL-Stage 3 and beyond). A power calculation was performed and a minimum total of 12 ROIs would be required to assess differences across organoids, assuming a Type I error rate of 5% and a Type II error rate of 20% (i.e., 80% Power). Thus, 4 ROIs were selected per organoid at random, from a total of 6 organoids from 3 independent differentiation experiments, resulting in 24 z-stack images (twice as many as needed). Absolute values of differences between HC and DBC maturation states (difference scores), within each ROI were calculated and utilized as the units of analysis. ROIs were numbered in order of difference scores, from lowest to highest, to assess variations in maturation patterns within each organoid. Analysis of Variance (ANOVA) was used to compare both average difference scores between organoids (inter-organoid variability) as well as average variations in difference scores within each organoid (intra-organoid variability). For this sub-analysis, statistical significance was assessed for each F-test at a level of 0.025 or lower.

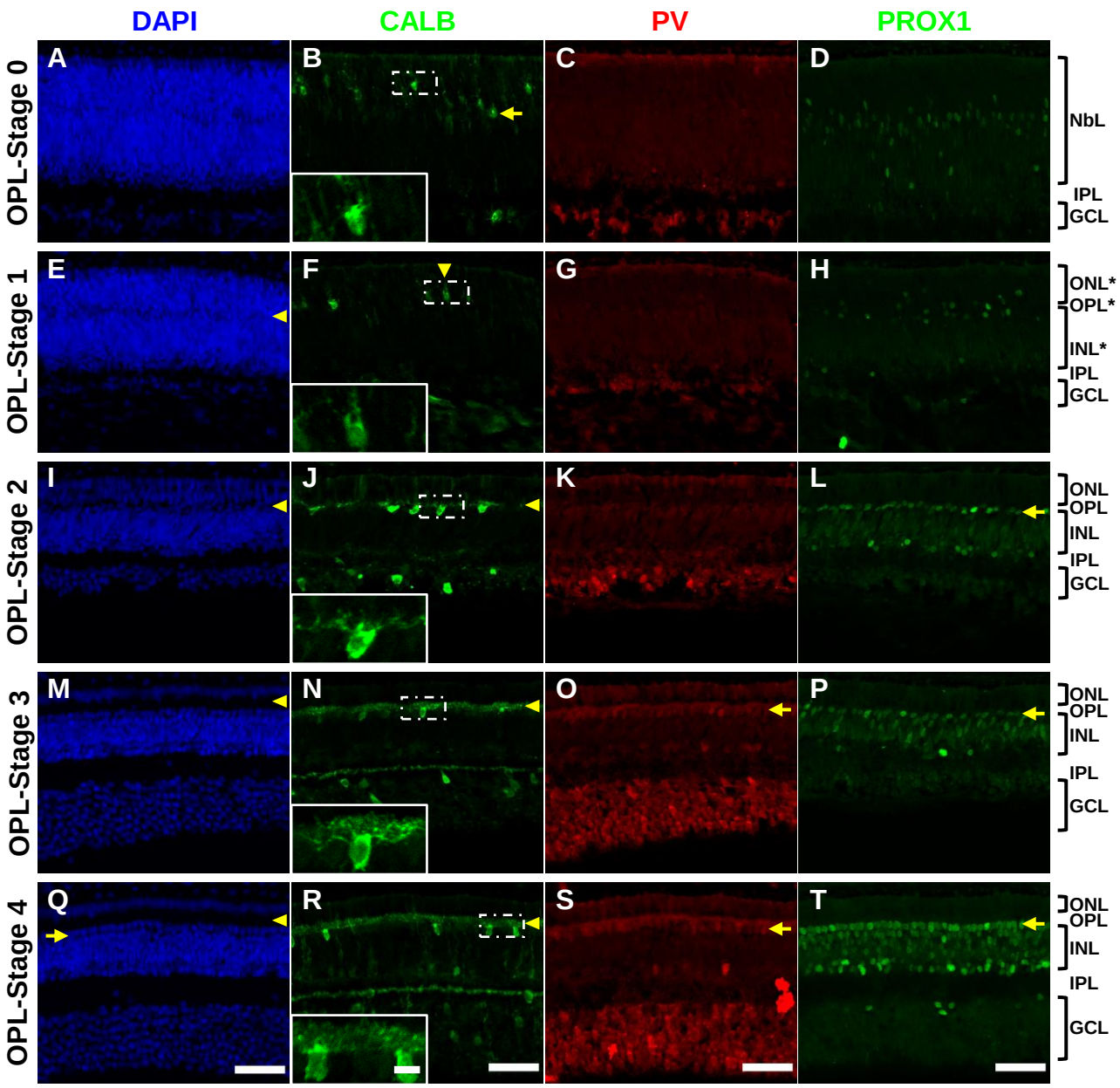

Fig. S1. Characterization of HCs in fetal week 16.6 (~D118) human retina with additional cellular markers. Representative immunofluorescence images of a fetal week 16.6 (~D118) retina showing HC nuclear lamination and morphogenesis at OPL-Stage 0 (A-D), OPL-Stage 1 (E-H), OPL-Stage 2 (I-L), OPL-Stage 3 (M-P) and OPL-Stage 4 (Q-T). CALB, PV and PROX1 markers were used to detect HCs. As these markers are not specific to HCs and are expressed by other retinal cell types, the spatial location of expression at the NbL in OPL-Stage 0, and basal aspects of nascent ONL in OPL-Stage 1 and distinct INL in OPL-Stage 2 to 4 guided confirmation of HC identity. DAPI, CALB and PV images shown here are from the same retinal section. PROX1 images are from serial sections where OPL stages were identified based on nuclear arrangement. Yellow arrows point out stage-specific features: spatial location of nascent $CALB^+$ HCs (B), and single row of $PROX1^+$ HCs (L,P,T), and PV^+ HCs (O,Q,S) at apical aspects of the INL. Yellow arrowheads point out other stage-specific features: developing OPL (E,I,M,Q) and $CALB^+$ HC processes (F,J,N,R). The boxes on CALB panel (B,F,J,N,R) indicate selected regions of interest and insets show them magnified. Of note, a subset of ganglion cells (B,F,J,N,R), amacrine cells (R) and Muller glia (R) expressed Calbindin. PV expression was detected in the ganglion cell layer in all stages, with a large population of PV^+ ganglion cells in OPL-Stage 3 and 4. A large population of INL cells expressed $PROX1^+$, along with a subset of ganglion cells. The same imaging parameters and signal enhancements were used for each marker across all stages. Abbreviations: NbL, neuroblastic layer; ONL, outer nuclear layer; OPL, outer plexiform layer; INL, inner nuclear layer; IPL, inner plexiform layer; GCL, ganglion cell layer. * indicates nascent layers. Scale bar: (A-T) 50 μm; (B,F,J,N,R insets, 8 μm).

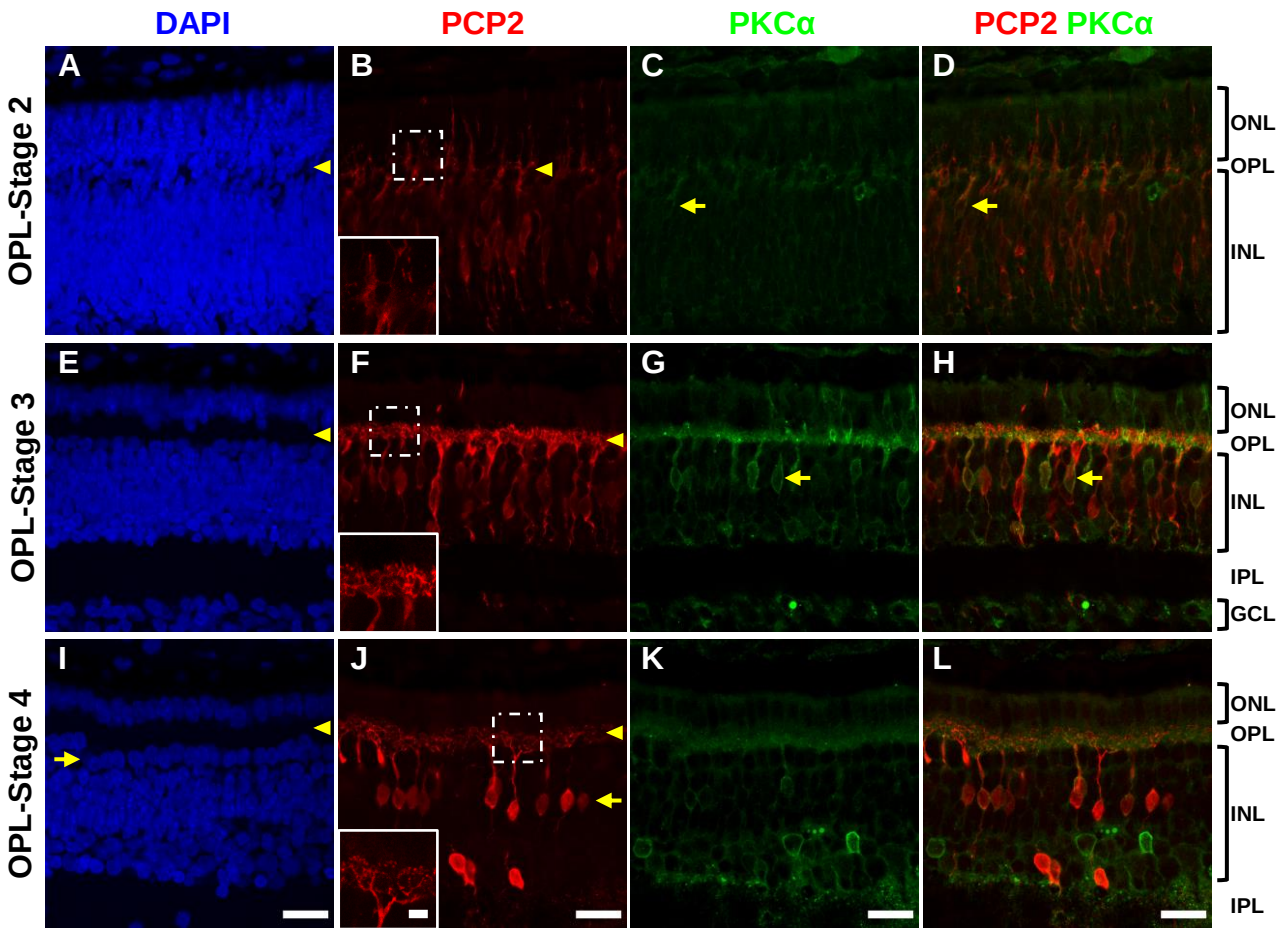

Fig. S2. Characterization of DBCs in fetal week 16.6 (~D118) human retina. Representative immunofluorescence images of a fetal week 16.6 (~D118) retina showing DBC morphogenesis and PKCα expression at OPL-Stage 2 (A-D), OPL-Stage 3 (E-H), and OPL-Stage 4 (I-L). Yellow arrows point at representative of DBCs expressing PKCα (C,D,G.H), single row of HC nuclei at apical aspects of INL characteristic of OPL-Stage 4 (I), and lateral arrangement of DBC cell bodies at OPL-Stage 4 (J). Yellow arrowheads point out stage-specific features: developing OPL (A,E,I) and DBC processes (B,F,J). The boxes in B, F, and J indicate selected regions of interest with accompanying magnified insets. Abbreviations: ONL, outer nuclear layer; OPL, outer plexiform layer; INL, inner nuclear layer; IPL, inner plexiform layer; GCL, ganglion cell layer. Scale bar: (A-L) 20 μm; (B,F,J insets, 8 μm).

A

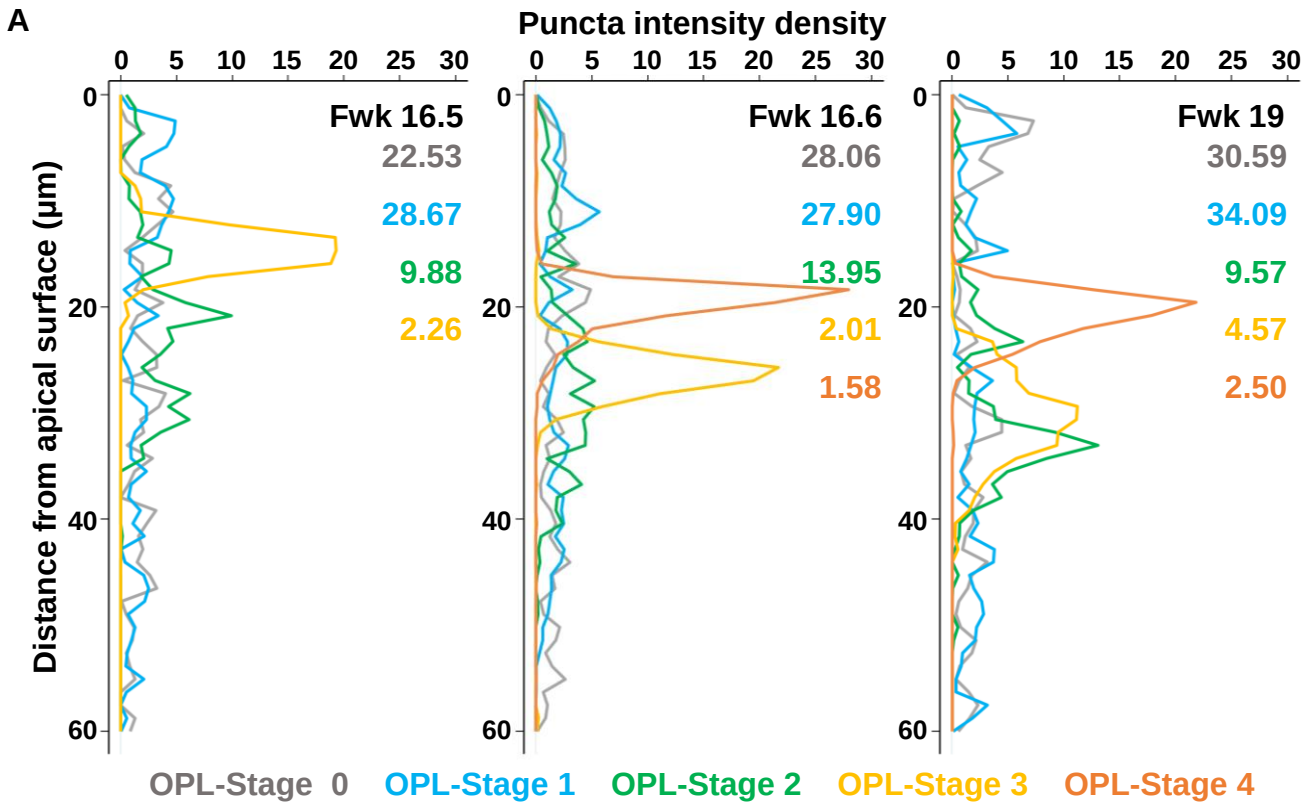

B Pairwise comparison of Bassoon puncta intensity distribution

Fwk 16.5

OPL stage	0	1	2
1	0.09		
2	<0.0001	<0.0001	
3	<0.0001	<0.0001	0.03

Fwk 16.6

OPL stage	0	1	2	3
1	0.94			
2	<0.0001	<0.0001		
3	<0.0001	<0.0001	<0.0001	
4	<0.0001	<0.0001	<0.0001	0.83

Fwk 19

OPL stage	0	1	2	3
1	0.21			
2	<0.0001	<0.0001		
3	<0.0001	<0.0001	0.07	
4	<0.0001	<0.0001	0.01	0.45

Fig. S3. Quantitative evaluation of Bassoon localization by OPL stage in fetal retinae based on automated detection of fluorescence intensity maxima. (A) Graphs showing Bassoon puncta intensity density distribution along apical-basal axis (y-axis =60 μm) on 2 μm-thick confocal slabs for OPL stages for three retinae at fetal weeks 16.5, 16.6 and 19. Average interquartile range (IQR) values for Bassoon intensity distributions are shown at the top right corner for each stage. n = 3 regions of interest analyzed per stage. The available tissue sections for fetal week 16.5 lacked OPL-Stage 4. An apical shift in the peak from OPL-Stage 3 to OPL-Stage 4 was observed due to the presence of only a single layer of photoreceptors in the parafoveal ONL. (B) Pair-wise comparison of Bassoon puncta intensity distribution between OPL stages within each fetal retina. The *p* value for pair-wise comparisons are shown in the table and non-significant values ($p>0.001$) are shown in blue.

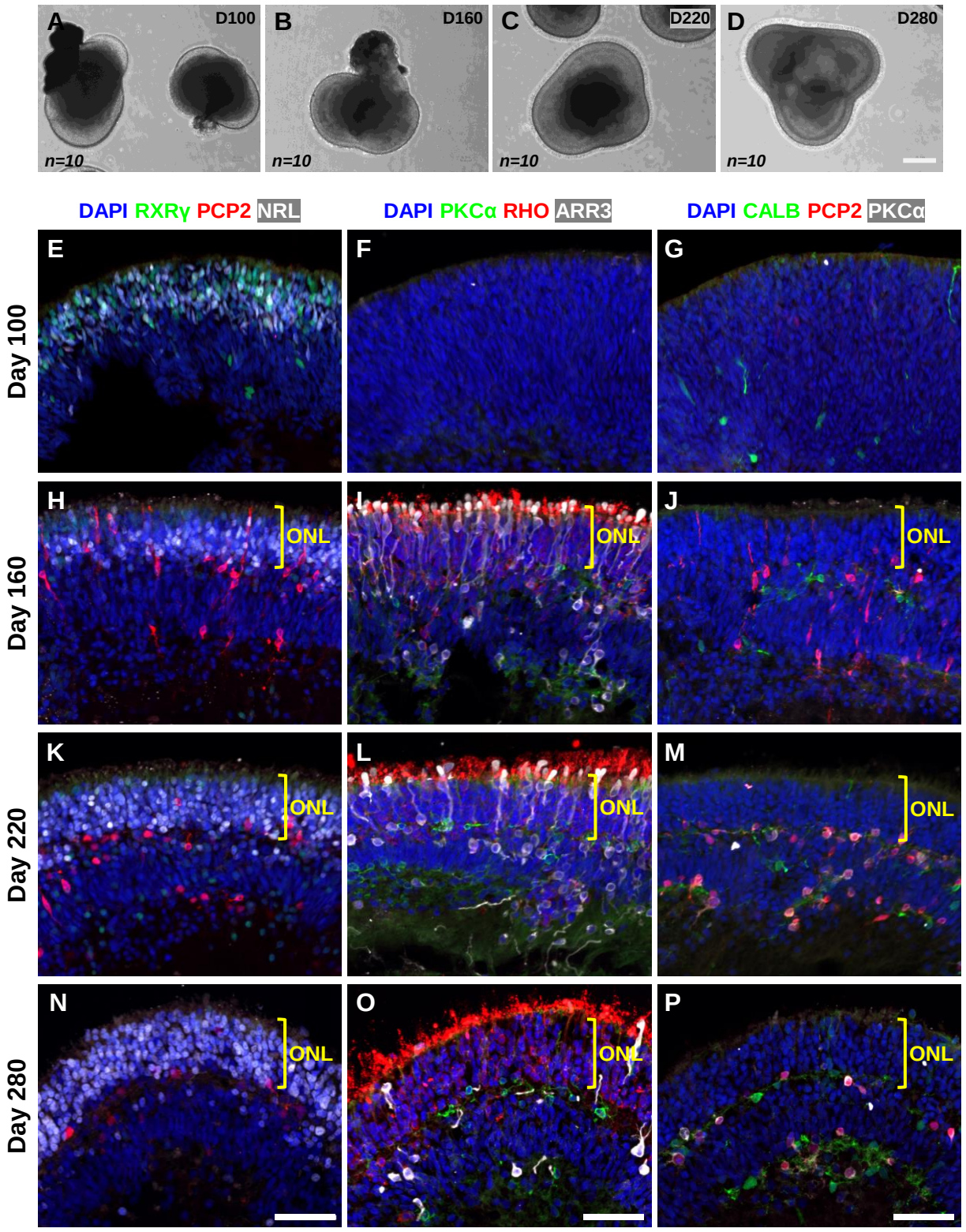

Fig. S4. Outer plexiform layer formation in H9 ESC-derived HROs. (A-D) Representative light microscopy images of live H9 HROs at four sampling ages: day 100 in culture (D100) (A), D160 (B), D220 (C) and D280 (D). (E-P) Immunofluorescence staining of H9 HROs at four ages. The retinal cell type specific antibodies used are same as in Fig. 5. Serial sections are shown at each age for three antibody panels. n=10, number of HROs evaluated at each age. Yellow brackets in H-P indicate ONL. Abbreviations: ONL, outer nuclear layer. Scale bar: (A-D) 300 μm; (E-P) 50 μm.

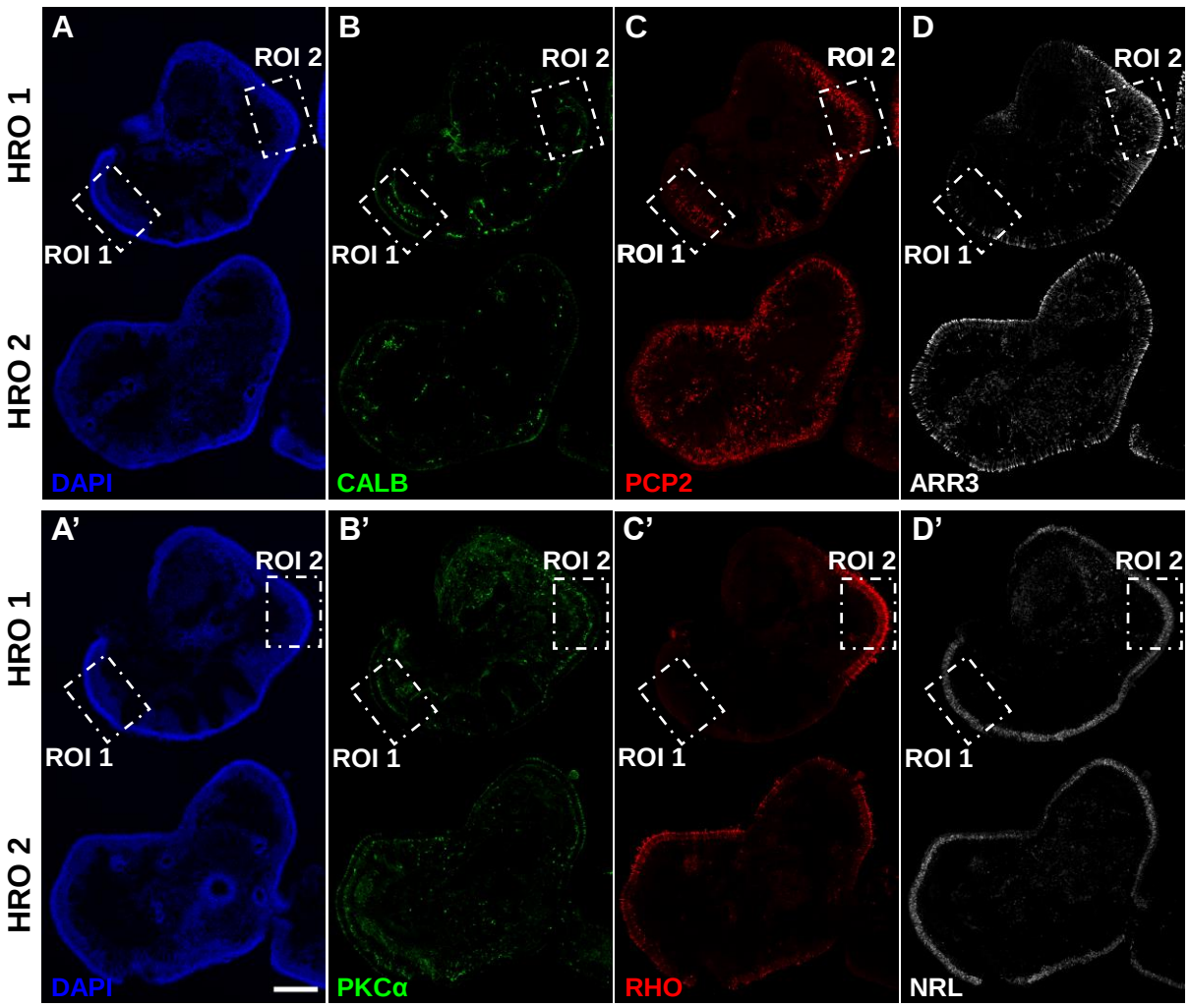

Fig. S5. Inter- and intra- organoid variability in cellular composition and maturational state of WTC11 iPSC-derived HROs. (A-D') Single channel images of WTC11 HROs at D160 shown in Fig. 6A-A'. The boxes on A-D' indicate selected regions of interest, ROI 1 and ROI 2. Scale bars: (A-D') 200 μm**.**

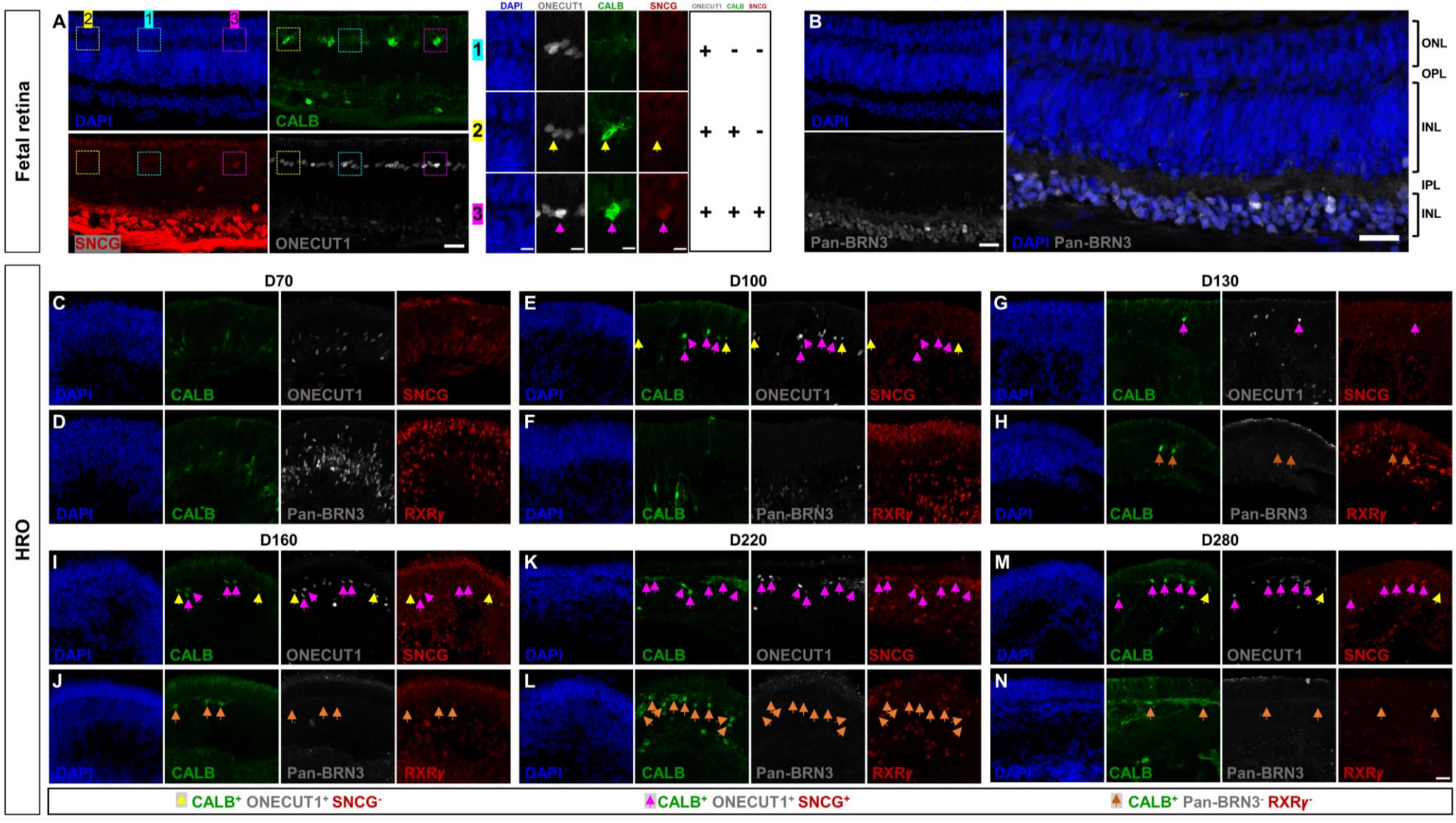

Fig. S6. Validation of cell type-specific markers on fetal retina and confirmation of horizontal cell identity, cone identity and progressive retinal ganglion cell loss in HROs. (A-B) Representative immunofluorescence images of a fetal week 16.6 (~D118) at OPL-Stage 2 showing the expression profiles of CALB, SNCG and ONECUT1 (A) and pan-BRN3 (B). HCs are present as a single row of cells along the apical aspect of the INL. All HCs were ONECUT1^{+}. A subset of ONECUT^{+} cells also expressed CALB, and subset of these expressed SNCG weakly as well. Robust SNCG expression was detected in the ganglion cell layer. Insets, arrows are color-coded based on specific combination of marker expression and indicate representative ONECUT1^{+}CALB^{-} SNCG^{-} cells (cyan), ONECUT1^{+}CALB^{+} SNCG^{-} cells (yellow) and ONECUT1^{+}CALB^{+}SNCG^{+} cells (magenta). (B) Unlike SNCG, pan-BRN3 expression was restricted to the ganglion cells, with no immunoreactivity in the ONL or INL. n=1 fetal retina. (C-N) Representative immunofluorescence images of HROs at ages D70 to D280 evaluating HC identity of CALB^{+} cells (C-N), cone identity of RXRγ^{+} cells (D,F,H,J,L,N) and progressive loss of RGCs (D,F,H,J,L,N). At D70, when HCs, cones, and RGCs are in close spatial proximity and their laminar organization is evolving, the spatial location and single maker expression of CALB and RXRγ is not enough to confirm HC and cone identities, respectively (C-D). There is progressive loss of RGCs during HRO development with drastic decrease from D70 (D) to D100 (F), culminating in only rare instances thereafter (H,J,L,N). Beginning from D130 and after, all CALB^{+} cells in the expected HC location express ONECUT1 (SNCG^{-}, yellow arrows or SNCG^{+}, magenta arrows in G,I,K,M) and lack BRN3 and RXRγ expression (orange arrows in H,J,L,N), thereby confirming their HC identity. Starting from D100, all RXRγ^{+} cells in the photoreceptor layer lack BRN3, thereby confirming their cone identity. Arrows are color-coded based on the specific combination of markers expressed as indicated in the legend at the bottom. Abbreviations: ONL, outer nuclear layer; OPL, outer plexiform layer; INL, inner nuclear layer, IPL, inner plexiform layer; GCL, ganglion layer. n=5 HROs from two independent HRO preparations at each age. Scale bar: (A-N) 25 μm; (A, inset) 8 μm.

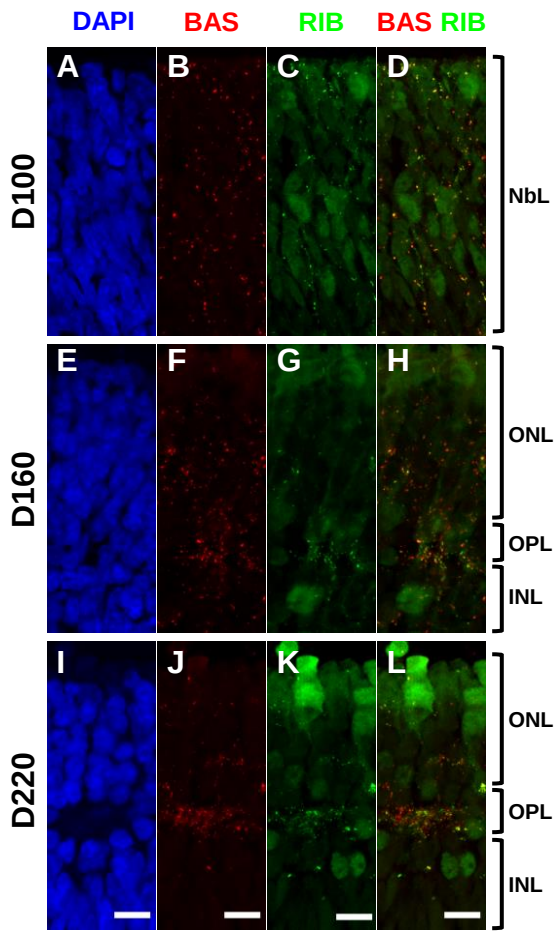

Fig. S7. Synaptic targeting of ribbon proteins, Bassoon and Ribeye, in H9 ESC-derived HROs. Representative maximum intensity projections of immunofluorescence images of H9-derived HROs at ages D100 (A-D), D160 (E-H) and D220 (I-K) showing progressive synaptic targeting of Bassoon and Ribeye to the OPL. Abbreviations: NbL, neuroblastic layer; ONL, outer nuclear layer; OPL, outer plexiform layer; INL, inner nuclear layer. Scale bar: (A-L) 10 μm.

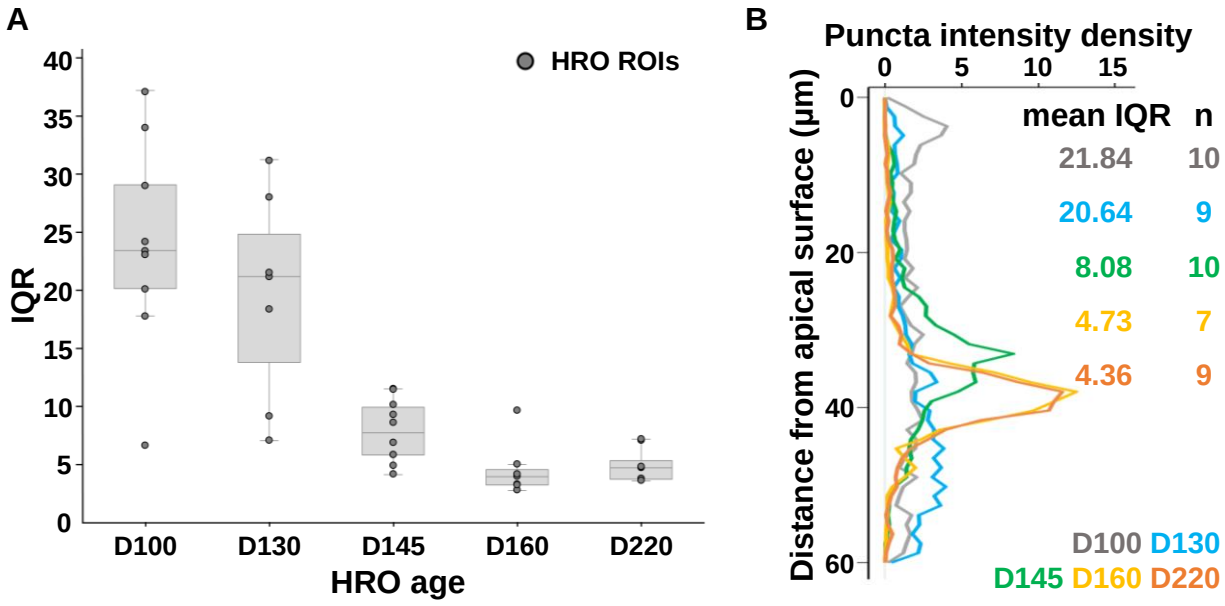

C Pairwise comparison of Bassoon puncta intensity distribution

		Fetal retina OPL stage				
		0	1	2	3	4
HRO age	D100	0.18	0.03	0.006	<0.0001	<0.0001
	D130	0.10	0.02	0.02	<0.0001	<0.0001
	D145	<0.0001	<0.0001	0.42	0.17	0.08
	D160	<0.0001	<0.0001	0.10	0.65	0.37
	D220	<0.0001	<0.0001	0.08	0.72	0.42

Fig. S8. Quantitative evaluation of Bassoon localization by OPL stage in WTC11 iPSC-derived HRO based on automated detection of fluorescence intensity maxima. (A-B) Bassoon intensity distributions along the apical-basal axis in a volume of 30 µm × 60 µm × 2.01 µm for regions of interest (ROIs) analyzed at each age, represented as a boxplot with individual IQR values plotted (A). Boxplot shows median values (middle bars), and first to third interquartile ranges (boxes); whiskers indicate 1.5 times the interquartile range; dots represent individual ROIs. (B) Intensity density graphical distribution showing puncta distribution along the apical-basal axis (y-axis =60 µm) for each age with mean IQR values listed at top right. n, number of regions analyzed at each age, were taken from 5, 5, 6, 4 and 4 HROs at D100, D130, D145, D160 and D220 respectively, from 3-4 independent HRO preparations. (C) Pair-wise comparison of Bassoon puncta intensity distribution between HRO ages and fetal retina OPL stages (data shown in Fig. S8B and Fig. S3A, respectively). The *p* values for pair-wise comparisons are tabulated with *p* values above adjusted significance cut-off of 0.001 indicated in blue.

Table S1. Antibodies used in the study.

Antibody	Source	Catalogue number	Dilution
Recoverin	EMD Millipore	AB5585	1:1000
RXRγ (Y20)	SCBT	sc-555	1:500
RXRγ (A2)	SCBT	sc-365252	1:200
Arrestin 3	NOVUS Biologicals	NBP1 37003	1:50
NRL	R&D Systems	AF2945	1:50
Rhodopsin (Clone RET-P1)	Millipore Sigma	MAB5316	1:30-1:50
Chx10 (N-18) (VSX2)	SCBT	sc-21690	1:500
PCP-2 (F3)	SCBT	sc-137064	1:100
PKCα (Y124)	Abcam	ab32376	1:1000
PKCα	R&D Systems	AF5340	1:50
Calbindin (D-28K)	Millipore Sigma	AB1778	1:500
Parvalbumin	Sigma-Aldrich	P3088-100UL	1:200
Prox-1	Angio-Bio	11-002	1:1000
HNF1/ONECUT1	R&D Systems	AF6277	1:300
SNCG	Abnova	H00006623	1:500
BRN3	SCBT	Sc-6026	1:500
Bassoon (SAP7F407)	ENZO Lifesciences	ADI VAM PS003	1:1000
Ribeye (CtBP2)	St John's Laboratory	STJ92514	1:1000
mGluR-6	St John's Laboratory	STJ94111	1:100-1:250
$Ca_V1.4$	Gift from Catherine W. Morgans		1:1000
Donkey anti Rabbit AF488	Invitrogen, ThermoFisher	A32731	1:1000
Donkey anti Mouse AF568	Invitrogen, ThermoFisher	A10037	1:1000
Donkey anti Goat AF647	Invitrogen, ThermoFisher	A32849	1:1000
Donkey anti Sheep AF647	Invitrogen, ThermoFisher	A21448	1:1000

Supplementary References

Holm, S. (1979). A Simple Sequentially Rejective Multiple Test Procedure. *Scand. J. Stat.* **6**, 65–70.

Schindelin, J., Arganda-Carreras, I., Frise, E., Kaynig, V., Longair, M., Pietzsch, T., Preibisch, S., Rueden, C., Saalfeld, S., Schmid, B., et al. (2012). Fiji: an open-source platform for biological-image analysis. *Nat. Methods* **9**, 676–682.